CHAPTER IV

Reduced graphene oxide (rGO)/PEDOT:PSS/ Manganese dioxide (MnO_2) ternary nanocomposite as anode catalyst for methanol oxidation

4.1 Introduction

From the last few decades, researchers have grown their interest to develop transition metal oxide (NiO, Cu_2O, ZnO, MnO_2, Co_3O_4) based catalyst due to their several oxidation states and heterogeneous catalytic activity [1-5]. Among these transition metal oxides, manganese dioxide (MnO_2) is drawing much attention due to low cost, environment friendliness, ease of synthesis, low operating voltage etc. [6]. Among different existing polymorphs of MnO_2, α-MnO_2 is extensively used in electrochemical energy storage systems due to its [2×2] tunnel structure along c-axis with MnO_6 octahedral units [7]. According to literature one-dimensional MnO_2 nanorods have long been used as electrode material in energy storage devices, sensor, catalysis, etc. due to enhancement of physical and chemical properties such as short diffusion path and easy electron transport [8]. However, the low conductivity (10^{-5} to 10^{-6} S cm^{-1}) of MnO_2 inhibits its application in energy storage and conversion devices. Many research groups are working on to overcome these drawbacks by making nanocomposites of MnO_2 with carbon based materials. Chunyang Jia et al. [9] synthesized MnO_2/poly(3,4-ethylenedioxythiophene)/multiwalled carbon nanotubes as electrode material for flexible micro-supercapacitor and obtained specific capacitance of 110 F g^{-1} at a current density of 2 A g^{-1}. Li Zhang et al. [10] synthesized Graphite/PEDOT/MnO_2 composites as electrode material for supercapacitor and they achieved power density of 90 W Kg^{-1} and 81.1% of retention capacity.

PEDOT:PSS (Poly(3,4-ethylenedioxythiophene):polystyrene sulfonate) is a conjugate polymer, where PSS is a polyelectrolyte that makes PEDOT soluble in water and carries a negative charge and PEDOT, the conjugate polymer carries a positive charge [11]. PEDOT/MnO_2 based nanostructured materials have been used as electrode materials in energy storage systems [12, 13]; however conducting polymer and metal oxides both exhibit poor cyclic stability. Previous reports show that incorporation of carbon allotropes

Baruah, B. and Kumar, A., *Synthetic Metals*, *245*:74-86, 2018.

may enhance the mechanical stability as well as electrochemical performance of the electrocatalyst [14].

Among the carbon compounds, two dimensional sp^2 hybridized monolayer graphene sheets have gained much attention due to large surface area, excellent electrical conductivity and high tensile strength [15, 16]. Reduced graphene oxide (rGO) has some advantage over graphene and other graphene derivatives as catalyst support in DMFCs due to the presence of defects and oxygen containing functional groups such as epoxy, hydroxyl, carboxylic groups on its edges and basal plane as well as low cost and large scale production [17]. Conducting polymer/copper nanoparticles supported rGO nanosheets show excellent electrocatalytic activity toward methanol oxidation [18]. Surya Prakash and co-workers [19] studied the effect of annealing temperature of Ni/rGO catalysts on urea oxidation. Joong Hee Lee et al. [20] synthesized $NiCo_2O_4$-RGO composite as an alternative to platinum catalyst and obtained oxidation potential of methanol at 0.6 V with higher anodic current density.

Recently, K. Hareesh et al. [21] synthesized PEDOT:PSS coated MnO_2 nanorods/rGO nanocomposite for electrode material in supercapacitor and they reported that dispersion of MnO_2/rGO in PEDOT:PSS matrix may allow edges and corners for charge storage and protect the binary material from dissolution in the electrolyte. PEDOT:PSS also stabilizes the MnO_2/rGO nanocomposite and enhances film formation capability [14]. Yulin Min et al. [22] synthesized MnO_2/GNRs/PANI ternary composites with porous structures by a two-step *in situ* polymerization method for supercapacitor electrode and achieved 472 F g^{-1} with capacitive retention 85%. De Yan et al. [23] also prepared MnO_2/rGO/PEDOT:PSS nanocomposite for electrode material in supercapacitor and achieved 169.1 F g^{-1} of specific capacitance and capacitive retention factor of 66.2% after 2000 cycles.

This chapter focuses on the application of rGO/PEDOT:PSS/MnO_2 ternary nanocomposite as an alternative to platinum anode catalyst towards methanol oxidation in alkaline media. To achieve the objectives of present work, initially MnO_2 nanorods were synthesized by hydrothermal route. Subsequently, rGO/PEDOT:PSS/MnO_2 ternary nanocomposite was synthesized by *in situ* polymerization method. The morphological characterizations of synthesized nanocomposite reveal the formation of rGO wrapped polymer coated MnO_2 nanorods, which inhibit the agglomeration of rGO nanosheets. Electrochemical characterization shows that rGO/PEDOT:PSS/MnO_2/ITO electrode exhibits lower onset potential, higher oxidation current density and better stability than that of PEDOT:PSS/MnO_2/ITO and MnO_2/ITO electrodes.

4.2 Morphological characterizations

4.2.1 Scanning electron microscopy

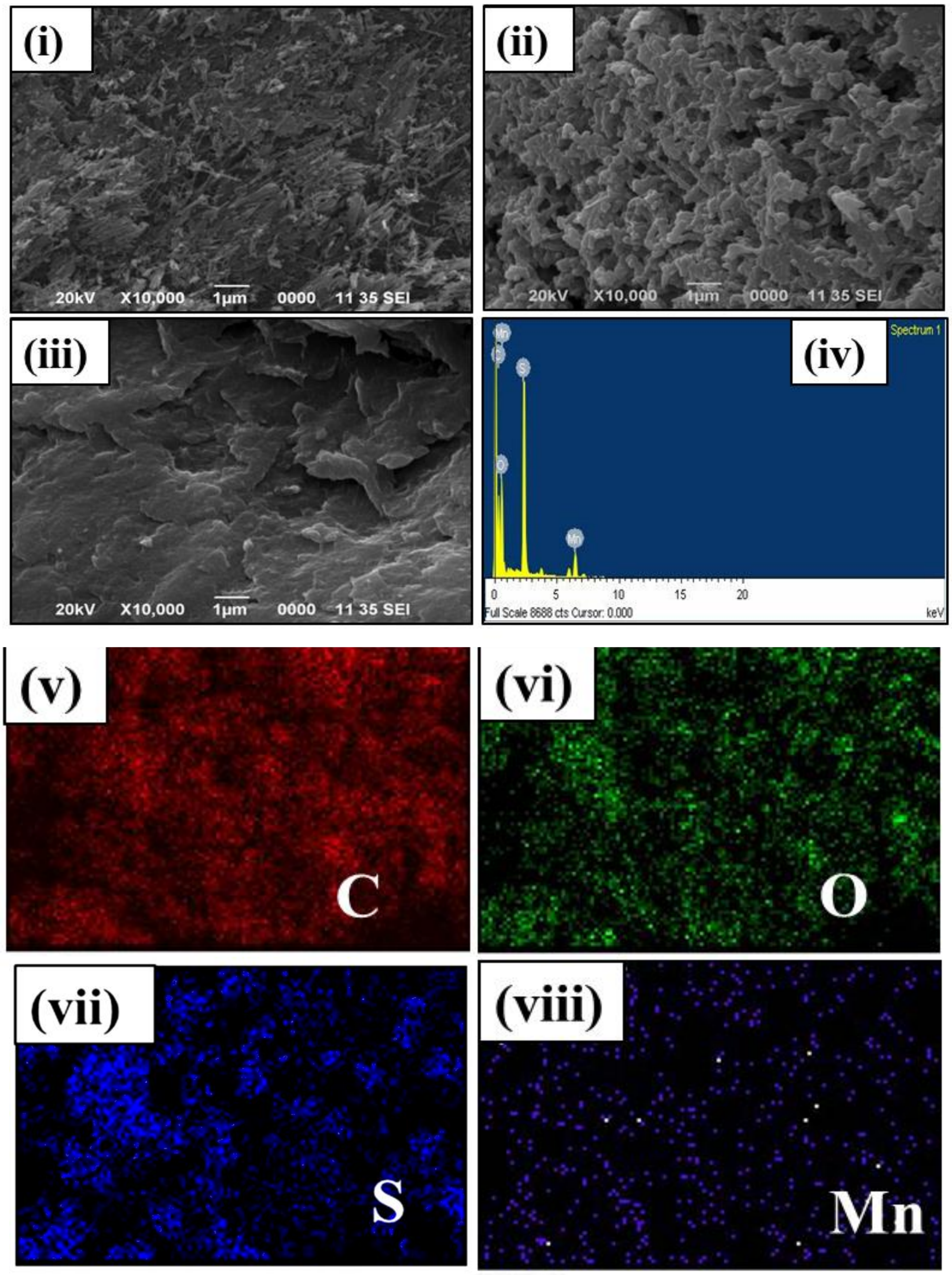

Figure 4.1: *SEM images of (i) MnO_2 nanorods, (ii) PEDOT:PSS/MnO_2 nanocomposite and (iii) rGO/PEDOT:PSS/MnO_2 nanocomposite and (iv) EDX spectrum of rGO/PEDOT:PSS/MnO_2 nanocomposite. Elemental mapping of rGO/PEDOT:PSS/MnO_2 nanocomposite for (v) C, (vi) O, (vii) S and (viii) Mn.*

Figures 4.1 (i), (ii) and (iii) show the SEM images of MnO_2 nanorod, PEDOT:PSS/MnO_2 and rGO/PEDOT:PSS/MnO_2 nanocomposites respectively. Figure 4.1 (i) depicts the SEM image of randomly oriented and densely packed porous networks of MnO_2 nanorods. In Figure 4.1 (ii), homogeneous distribution of polymer coated bundle of MnO_2 nanorods are observed however in Figure 4.1 (iii), these nanorod structures are not visible due to wrapping of polymer coated nanorods by rGO nanosheets. The possible reason of the observed nanostructure may be due to van der Waals interaction between rGO plane and conducting polymer which enhances the growth of rGO nanosheet over the polymer coated nanorods [24]. From EDX spectrum (Figure 4.1 (iv)), the presence of manganese (Mn), carbon (C), oxygen (O) and sulfur (S) is confirmed in rGO/PEDOT:PSS/MnO_2 nanocomposite. In EDX, higher elemental contribution (44.73 wt.%) comes from C due to presence of rGO and PEDOT. Significant amounts of O (41.74 wt.%), Mn(1.61 wt.%) and S (11.92 wt.%) are also observed due to presence of MnO_2 and PSS. Elemental mapping of rGO/PEDOT:PSS/MnO_2 nanocomposite reveals uniform distribution of C, O, S and Mn in the nanocomposite as shown in Figures 4.1 (v)-(viii), however, distribution of carbon and oxygen is higher than that of sulfur and manganese.

4.2.2 Transmission electron microscopy

Microstructural investigations of rGO, MnO_2, PEDOT:PSS/MnO_2 and rGO/PEDOT:PSS/MnO_2 nanocomposites have been done by TEM as shown in Figure 4.2. In Figure 4.2 (i), few layers of crumpled paper like rGO nanosheets are observed [25]. Figures 4.2 (ii) and (iii) confirm the formation of MnO_2 nanorods with diameter range from 10-50 nm and length within 100-300 nm. Figures 4.2 (iv) and (v) reveal the formation of thick shell of PEDOT:PSS wrapped MnO_2 nanorods. The TEM images of rGO/PEDOT:PSS/MnO_2 nanocomposite (Figures 4.2 (vi) and (vii)) show that polymer coated MnO_2 nanrods are embedded within rGO nanosheets which is consistent with SEM results. The morphology of MnO_2 nanorods are well maintained even after polymer coating and incorporation of rGO. As observed from Figures 4.2 (vi) and (vii), the porous network of polymer coated MnO_2 nanorods are interconnected by conductive rGO nanosheet which enhances electrochemical performance of the electrocatalyst.

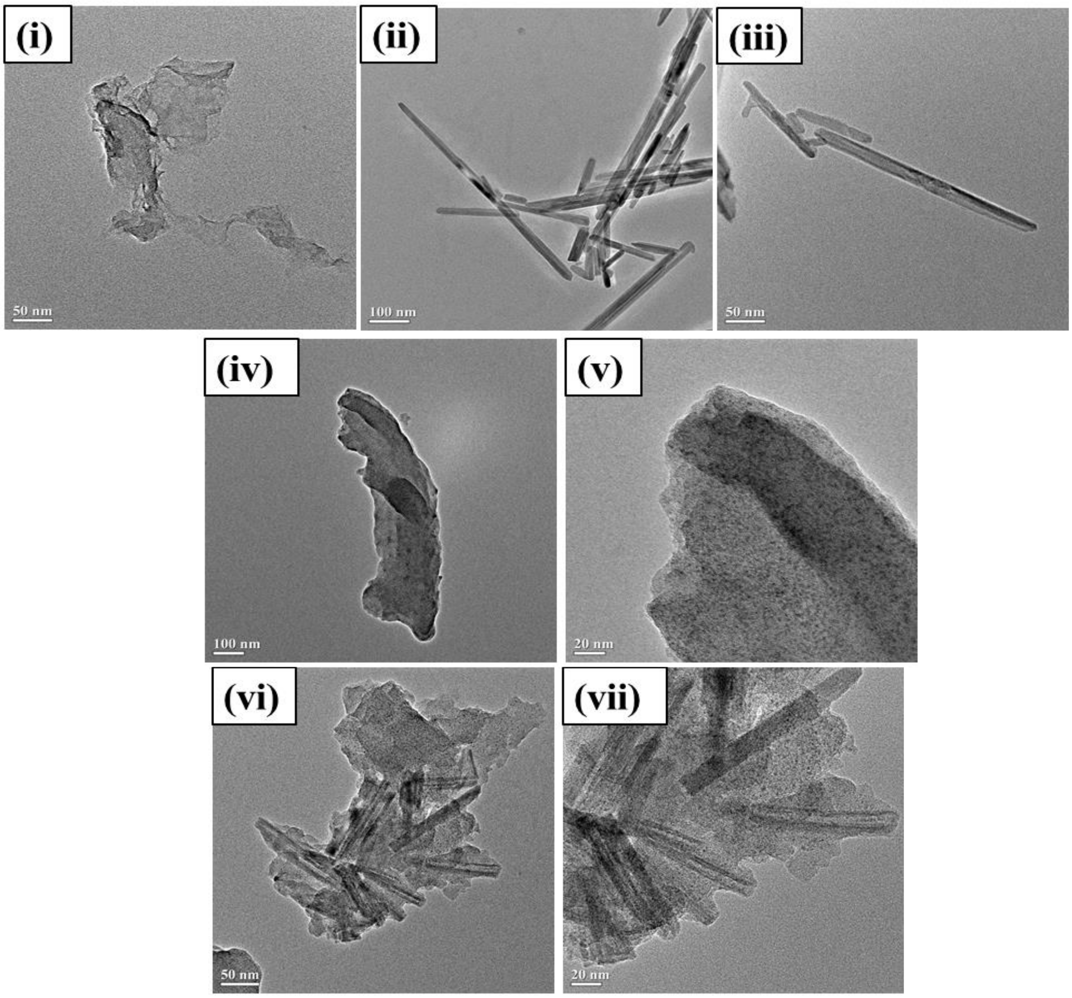

Figure 4.2: *TEM images of (i) rGO nanosheet, (ii)-(iii) MnO_2 nanorods, (iv)-(v) PEDOT:PSS/MnO_2 nanocomposite and (vi)-(vii) rGO/PEDOT:PSS/MnO_2 nanocomposite.*

4.3 Physical Characterizations

4.3.1 X-ray diffraction

The crystallinity of synthesized samples is investigated by XRD in the 2θ range of 0^o to 70^o. XRD patterns of GO and rGO are presented in Figure 4.3 (i). Figure 4.3 (ii) depicts the XRD analysis of MnO_2, PEDOT:PSS, PEDOT:PSS/MnO_2 and rGO/PEDOT:PSS/MnO_2 nanocomposites. The GO peak at 10^o with interlayer spacing of 0.88 nm corresponds to (002) plane [26]. On chemical reduction with hydrazine hydrate, the GO peak shifts to 25^o with interlayer spacing of 0.35 nm [24]. Decrease in interlayer spacing between rGO nanosheets indicates successful removal of oxygen containing groups during reduction of GO. One small rGO peak is observed around 43° due to turbostratic disorder of carbon materials [27]. Characteristic peaks of MnO_2 nanorods observed at 12.7°, 18°, 28.7°, 37.4°, 42°, 49.7°, 56°, 60° and 65.2° are well indexed to reflections from (110), (200), (310), (211), (301), (411), (600), (521) and (002) crystal planes of α- MnO_2 nanorod, respectively [21]. These XRD peaks correspond to tetragonal phase of α-MnO_2 nanorod as confirmed by standard data of JCPDS no. 44-0141 [28]. The broad peak of PEDOT:PSS around 26° corresponding the reflection from (010) plane appears due to interchain planar ring stacking distance [29]. The intensity of characteristic peaks of MnO_2 nanorod decreases sharply in PEDOT:PSS/MnO_2 nanocomposite. However a small intense broad peak ranging from 20.2° to 30° appears due to successful *in situ* polymerization of PEDOT:PSS over MnO_2 nanorods. A broad diffraction peak around 24.5° appears in rGO/PEDOT:PSS/MnO_2 nanocomposites due to overlapping of (010) plane of PEDOT:PSS and (002) plane of rGO. The characteristic XRD peaks of MnO_2 nanorods disappear in the ternary nanocomposite upon incorporation of PEDOT:PSS and rGO and the nanocomposite becomes amorphous [30]. This suggests that MnO_2 nanorods are uniformly coated by PEDOT:PSS and wrapped-up in rGO nanosheets [31, 32] as corroborated with SEM results (Figure 4.1 (iii)).

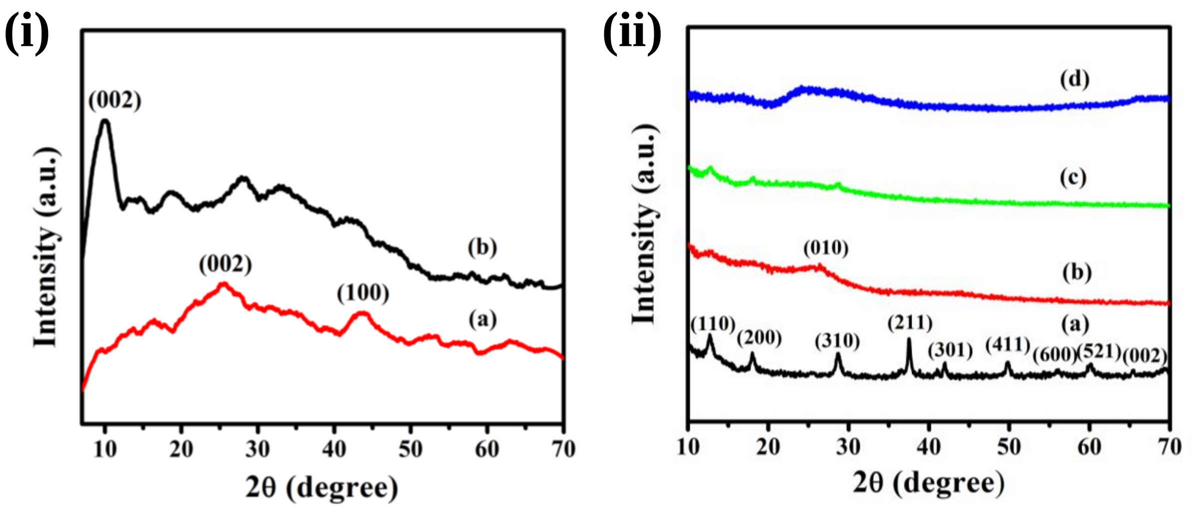

Figure 4.3: *(i) XRD patterns of (a) rGO and (b) GO, (ii) XRD patterns of (a) α-MnO_2 nanorods, (b) PEDOT:PSS (c) PEDOT:PSS/MnO_2 nanocomposite and (d) rGO/PEDOT:PSS/MnO_2 ternary nanocomposite.*

4.3.2 Raman spectroscopy

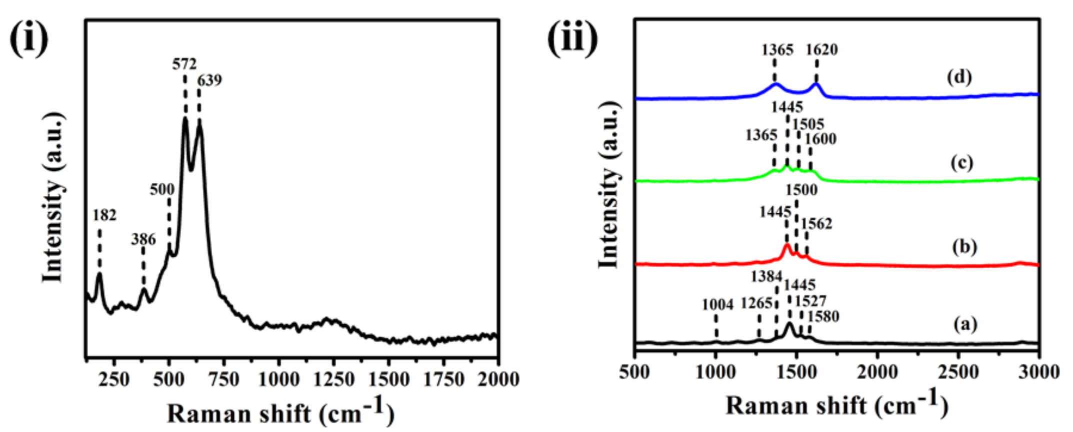

Figure 4.4: *(i) Raman spectrum of α-MnO_2 nanorod, (ii) Raman spectra of (a) PEDOT:PSS, (b) PEDOT:PSS/MnO_2 nanocomposite, (c) rGO/PEDOT:PSS/MnO_2 ternary nanocomposite and (d) rGO.*

Figure 4.4 (i) represents Raman spectrum of α-MnO_2 nanorod and Figure 4.4 (ii) shows Raman spectra of PEDOT:PSS, rGO, PEDOT:PSS/MnO_2 and rGO/PEDOT:PSS/MnO_2 nanocomposites. In Figure 4.4 (i), the Raman band at 572 cm^{-1} corresponds to Mn-O stretching vibration in the basal plane of MnO_6 sheets while the band at 639 cm^{-1} appears due to the symmetric stretching vibration (Mn-O) of MnO_6 groups [33]. The Raman band at 182 cm^{-1} can be attributed to an external vibration that obtained from the translational motion of MnO_6 octahedral [28]. The Raman bands at 386 and 500 cm^{-1} are related to lattice vibrations of Mn-O in MnO_2 [34]. The characteristic Raman band of PEDOT:PSS at 1004 cm^{-1} corresponds to C-S aliphatic stretching vibration mode of PSS [35]. The sharp peak at 1445 cm^{-1} in curve (a) of Figure 4.4 (ii) is related to C_α=C_β symmetrical stretching vibration [36]. The Raman bands at 1527 cm^{-1} and 1580 cm^{-1} appear due to the C_α=C_β asymmetrical stretching vibration that related to thiophene rings in the middle and at the end of PEDOT chains, respectively [36]. The small intense Raman bands at 1265 and 1384 cm^{-1} are associated with C_α-C_α inter ring stretching vibrations and C_β-C_β stretching deformations, respectively [37]. In Raman spectrum of PEDOT:PSS/MnO_2 nanocomposite (curve (b)), the presence of characteristic Raman bands of PEDOT:PSS indicates successful formation of the composite. The characteristic peaks of rGO i.e. D band at 1365 cm^{-1} is related to breathing modes of carbon with A_{1g} symmetry which indicates the presence of defects and disorder in rGO while the G band at 1620 cm^{-1}

corresponds to first order scattering from E_{2g} phonon modes of sp^2 bonded C atoms in rGO sheets [38, 39]. In Raman spectrum of rGO/PEDOT:PSS/MnO_2 nanocomposite, the characteristic peaks of both PEDOT:PSS and rGO are observed, however the Raman bands of α-MnO_2 nanorods disappear in both PEDOT:PSS/MnO_2 and rGO/PEDOT:PSS/MnO_2 nanocomposites due to wrapping of nanorods by PEDOT:PSS and rGO nanosheets, which is consistent with SEM and XRD results.

4.3.3 X-ray photoelectron spectroscopy

XPS has been performed to investigate the composition of surface, chemical oxidation and electronic states of rGO/PEDOT:PSS/MnO_2 nanocomposite. Figure 4.5 (i) presents full-scan survey spectra of α-MnO_2 nanorod and rGO/PEDOT:PSS/MnO_2 nanocomposite. The appearance of C 1s (286.2 eV), O 1s (532.5 eV), Mn 2p (640-660 eV) and S 2p peaks (162-172 eV) in the survey spectrum of ternary nanocomposite confirms the presence of these elements in the composite. The prominent peaks of O 1s and Mn 2p are observed in the full scan spectrum of α-MnO_2. The spectra are analysed using a peak fit program and the peak deconvolution is performed. The peaks have been deconvoluted to Gaussian components using the appropriate positions. The individual spectrum of Mn 2p (Figure 4.5 (ii)) shows two peaks at 643 eV and 654.7 eV corresponding to Mn $2p_{3/2}$ and Mn $2p_{1/2}$ spin orbit peaks of MnO_2, respectively with a separation energy of 11.7 eV. A shake up peak is observed at a binding energy centred at 646.3 eV due to Coulomb interactions between the 3d orbital electrons of transition metal and the ligand O 2p [40]. The Gaussian fit of C 1s core-level spectrum of the nanocomposite (Figure 4.5 (iii)) shows three peaks: nonoxygenated C-C (284.7 eV), C-O (286.1 eV) and C=O (288.6 eV). The O 1s spectrum of the composite (Figure 4.5 (iv)) shows two peaks. The two peaks at 531.4 eV and 533.1 eV are attributed to O species of hydroxyl group bonded with manganese (Mn-O-H) in MnO_2 and adsorbed water (H-O-H), respectively. Two prominent XPS peaks are observed in S 2p spectrum as shown in Figure 4.5 (v) implying the presence of sulfur atoms from both PEDOT and PSS. The deconvoluted peaks at 163.8 and 165 eV are attributed to S $2p_{3/2}$ and S $2p_{1/2}$ electronic configurations of thiophene ring in PEDOT [41], while the peaks at 167.9 eV corresponds to electronic state S $2p_{3/2}$ of sulfonate and at 168.4 eV is assigned to S $2p_{1/2}$ of sulfonic acid groups in PSS [41].

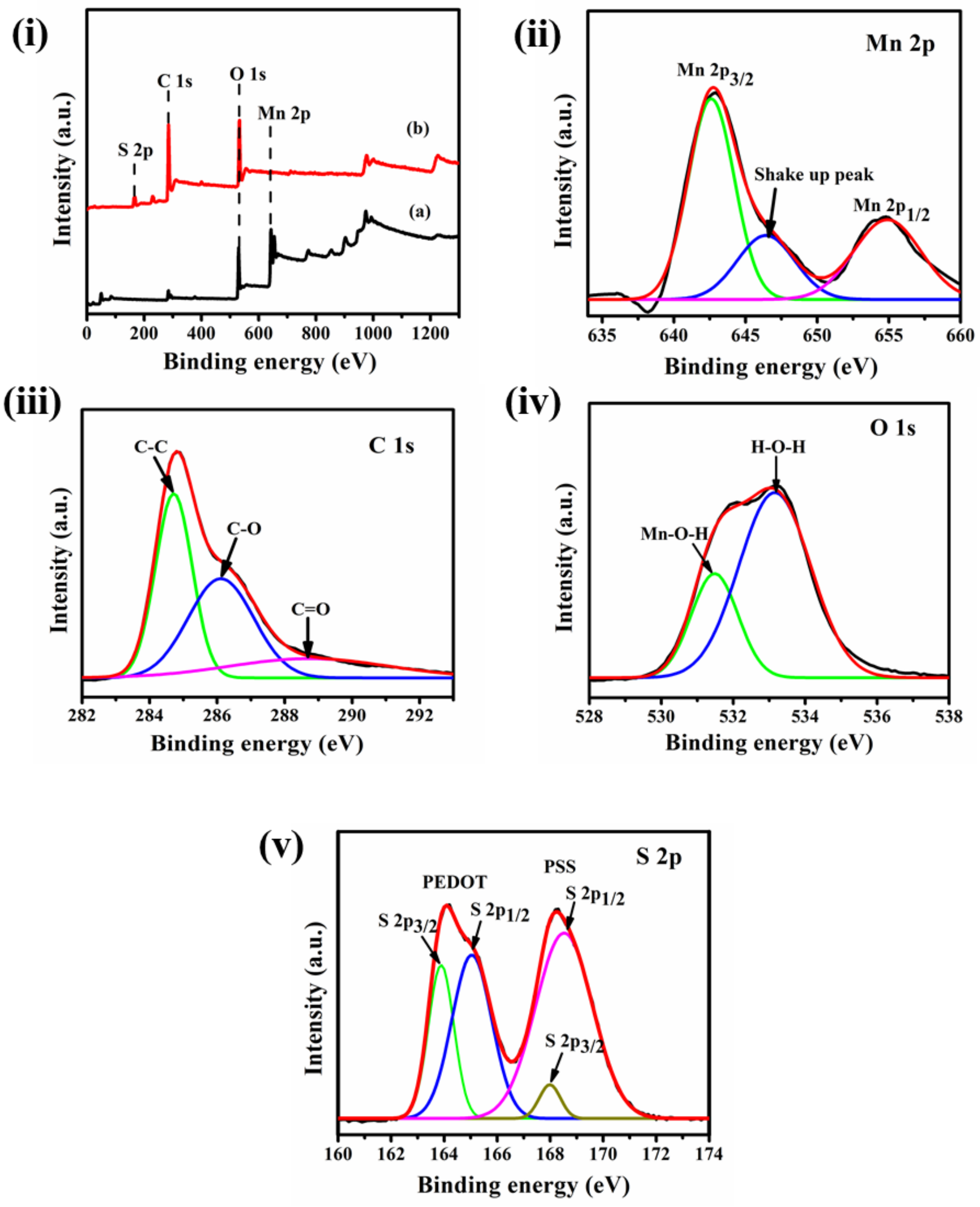

Figure 4.5: *(i) XPS survey spectra of (a) α-MnO*$_2$ *nanorod and (b) rGO/PEDOT:PSS/MnO*$_2$ *nanocomposite. High resolution XPS profile of (ii) Mn 2p, (iii) C 1s, (iv) O 1s and (v) S 2p of rGO/PEDOT:PSS/MnO*$_2$ *nanocomposite.*

4.3.4 Nitrogen (N_2) adsorption-desorption analysis

(i)

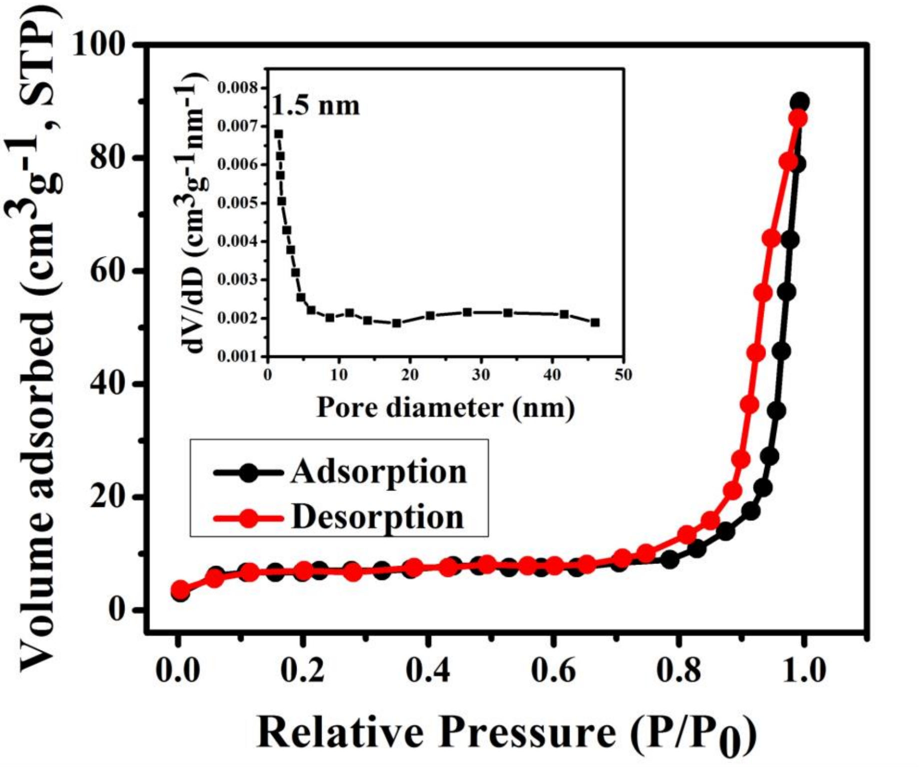

(ii)

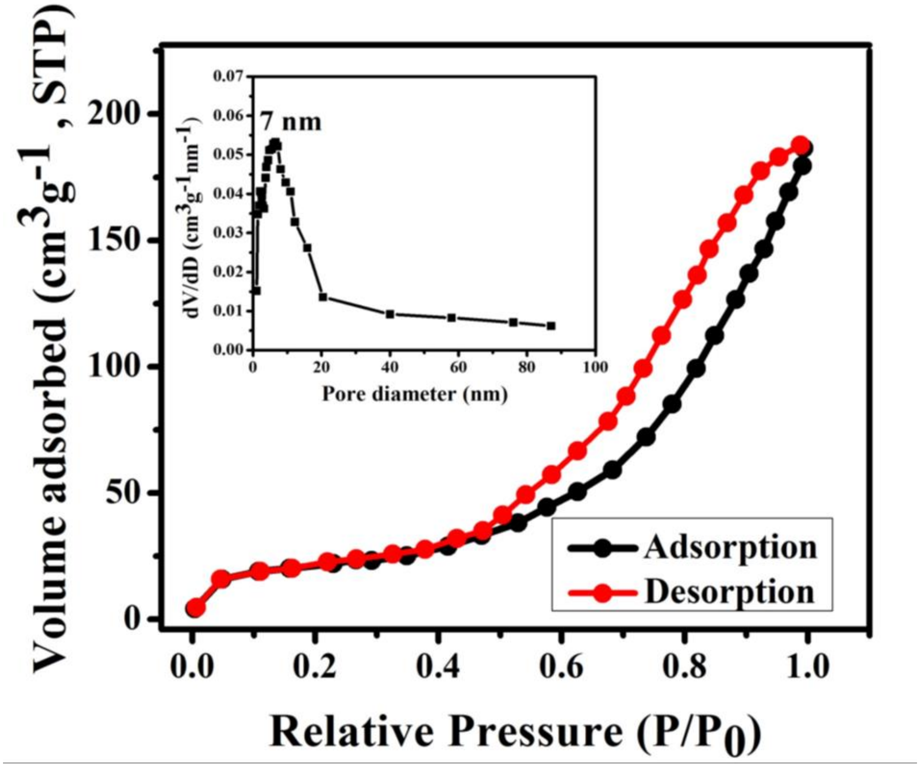

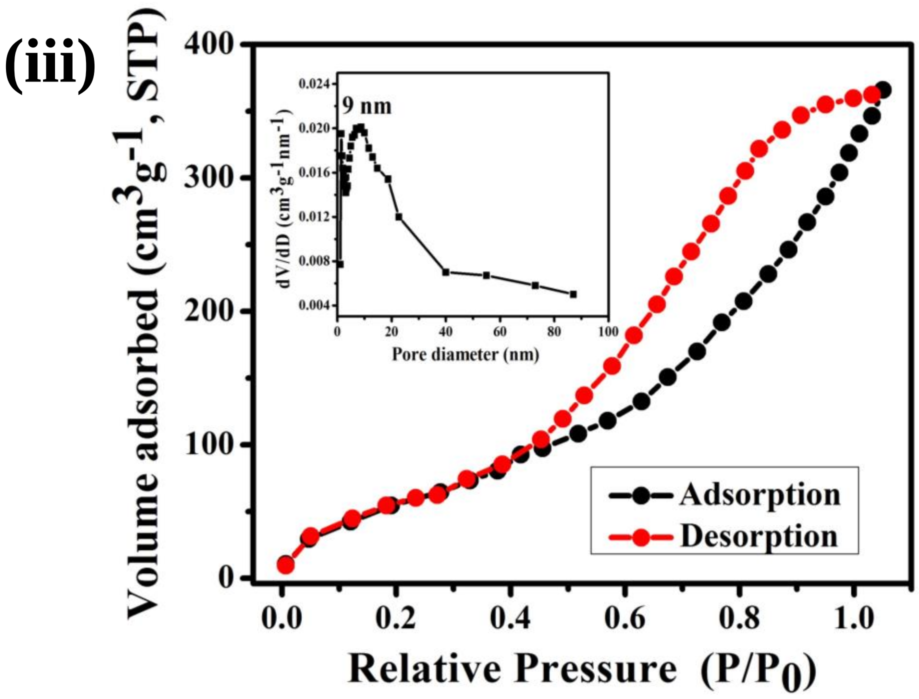

Figure 4.6: *N_2 adsorption-desorption isotherms of (i) MnO_2 nanorods, (ii) PEDOT:PSS/MnO_2 nanocomposite and (iii) rGO/PEDOT:PSS/MnO_2 ternary nanocomposite. Pore size distributions of the corresponding curves are shown in inset.*

Figure 4.6 displays the nitrogen adsorption-desorption isotherms and pore size distribution curves (inset) of MnO_2, PEDOT:PSS/MnO_2 and rGO/PEDOT:PSS/MnO_2 nanocomposites. The surface area of synthesized samples have been calculated using Brunauer-Emmett-Teller (BET) method at 77 K. Pore size distribution curves have been plotted from desorption isotherm using Barrett-Joyner-Halenda (BJH) method. Surface areas of the samples are calculated from Brunauer-Emmett-Teller method within the relative pressure range (P/P_0) of 0.05 to 0.3 P/P_0 and pore volume is calculated from single point measurement at a relative pressure of 0.95 P/P_0 [42]. Figure 4.6 (i) shows that MnO_2 nanorods exhibit hysteresis loop beyond the relative pressure range of 0.8 P/P_0 indicating type II isotherm. From the inset of Figure 4.6 (i), average distribution of pore size is observed at 1.5 nm indicating the presence of slit shaped micropores [8]. The hysteresis loops of PEDOT:PSS/MnO_2 and rGO/PEDOT:PSS/MnO_2 nanocomposites fall in the range from 0.5-1 P/P_0 and 0.4-1 P/P_0 implying type IV isotherms. The broad hysteresis loop of rGO/PEDOT:PSS/MnO_2 ternary nanocomposites suggests the presence of large concentration of mesopores which is consistent with that reported in literature [21]. From pore size distribution curves, it is observed that mesopore sizes of

PEDOT:PSS/MnO_2 nanocomposite and rGO/PEDOT:PSS/MnO_2 ternary nanocomposite fall within the range of 3-20 nm and 3-40 nm, respectively. The surface area of the ternary nanocomposite is observed to be enhanced (190 m^2 g^{-1}) than that of PEDOT:PSS/MnO_2 nanocomposite (76 m^2 g^{-1}) and MnO_2 nanorods (56 m^2 g^{-1}) due to large specific area of rGO nanosheets. The pore volume of ternary nanocomposite is larger (0.55 cm^3 g^{-1}) than that of PEDOT:PSS/MnO_2 nanocomposite (0.28 cm^3 g^{-1}) and MnO_2 nanorods (0.11 cm^3 g^{-1}). The mesoporous nature of the ternary nanocomposite results in shortening of ion diffusion path that leads to easy penetration of the electrolytes into the electroactive sites present in the electrocatalyst [43].

4.4 Electrochemical characterizations

4.4.1 Electrochemical activity of the modified electrodes

Figure 4.7 (i) depicts CVs of MnO_2/ITO, PEDOT:PSS/MnO_2/ITO and rGO/PEDOT:PSS/MnO_2/ITO electrodes in 0.5 M NaOH at scan rate 50 mV s^{-1}. All the modified electrodes exhibit a pair of redox peaks within the range from -0.35 V to +0.35 V due to Mn^{3+}/Mn^{4+} redox couple. The redox peaks appear due to following reactions [44]:

$$\mathrm{MnO_2 + e^- + H_2O \rightarrow MnOOH + OH^-} \qquad \text{(Cathode)} \qquad [4.1]$$

$$\mathrm{MnOOH - e^- + OH^- \rightarrow MnO_2 + H_2O} \qquad \text{(Anode)} \qquad [4.2]$$

The peak to peak separation (ΔE_p) value for rGO/PEDOT:PSS/MnO_2/ITO electrode is comparatively less (170 mV) than that of PEDOT:PSS/MnO_2/ITO (185 mV) and MnO_2/ITO (217 mV) electrodes. Fine dispersion of polymer coated MnO_2 nanorods over the highly conductive rGO nanosheets leads to fast electron transfer between the electrode and electrolyte, which is the possible reason for exhibiting highest current and narrowest ΔE_p value by rGO/PEDOT:PSS/MnO_2/ITO electrode. The enclosed area under the CV curve of rGO/PEDOT:PSS/MnO_2/ITO electrode is also larger than that of the other two electrodes implying better electrochemical performance of rGO/PEDOT:PSS/MnO_2/ITO electrode.

4.4.1.1 Variation of anodic peak current (I_{pa}) and cathodic peak current (I_{pc}) vs. scan rate rate (v)

Figures 4.7 (ii), (iii) and (iv) represent CVs of the modified electrodes in 0.5 M NaOH within the scan rate of 10-100 mV s^{-1}. The Figures show that the anodic and cathodic peak currents increase with increase in scan rate as well as anodic peak shifts toward positive side and cathodic peak shifts toward negative side indicating quasi-reversible or irreversible redox reactions caused by increase in internal resistance of the electrode [45, 46].

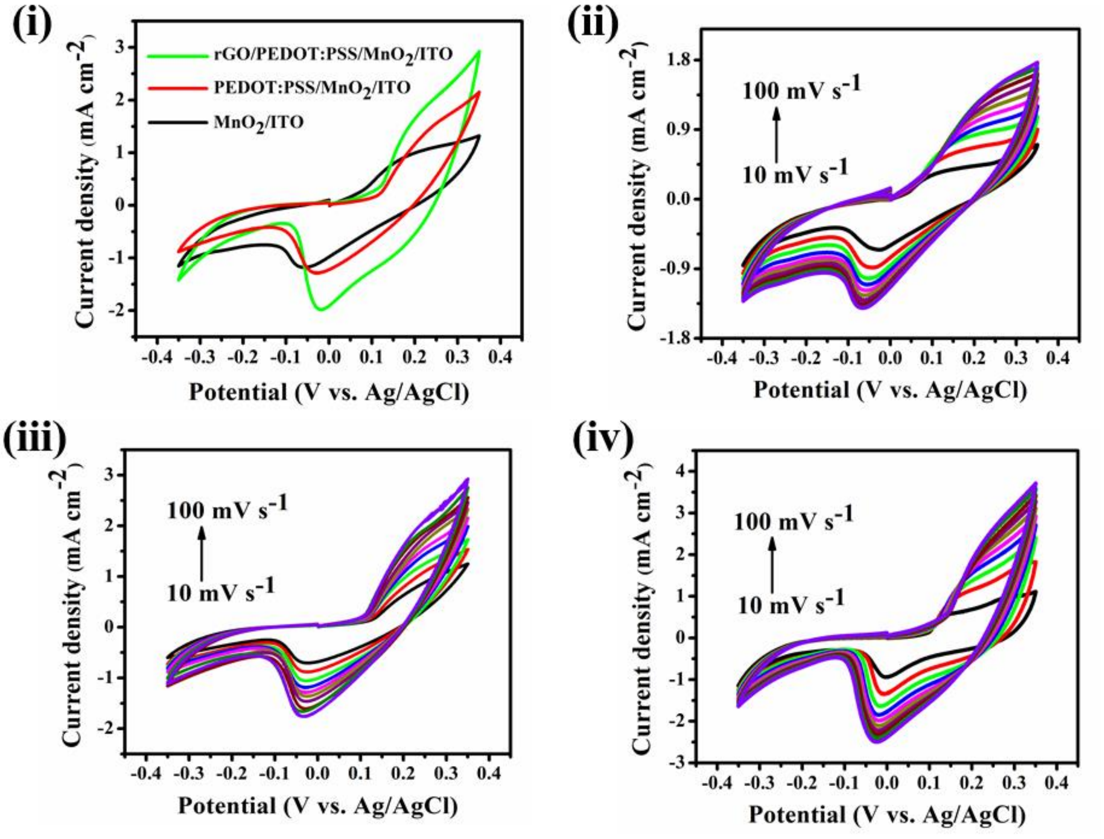

Figure 4.7: *(i) Cyclic voltammograms of MnO_2/ITO, PEDOT:PSS/MnO_2/ITO and rGO/PEDOT:PSS/MnO_2/ITO electrodes at a scan rate of 50 mV s^{-1}. Cyclic voltammograms of (ii) MnO_2/ITO, (iii) PEDOT:PSS/MnO_2/ITO and (iv) rGO/PEDOT:PSS/MnO_2/ITO electrodes at scan rates of 10-100 mV s^{-1} in 0.5 M NaOH solution.*

The anodic and cathodic peak current densities are linearly proportional to scan rates upto 40 mV s^{-1} as shown in Figure 4.8, indicating electrochemical behaviour of the redox couple [47]. Surface coverage (r^*) of the redox species Mn^{3+}/Mn^{4+} over the electrode surface can be calculated using slope (I_p/ν) of these two lines and Brown-Anson model [47], given by the equation,

$$I_p = \frac{n^2F^2r^*A\nu}{4RT} \qquad [4.3]$$

Where, n is the number of electrons involved in the process, F is Faraday constant, A is area of the electrode, ν is scan rate, R is gas constant and T is temperature.

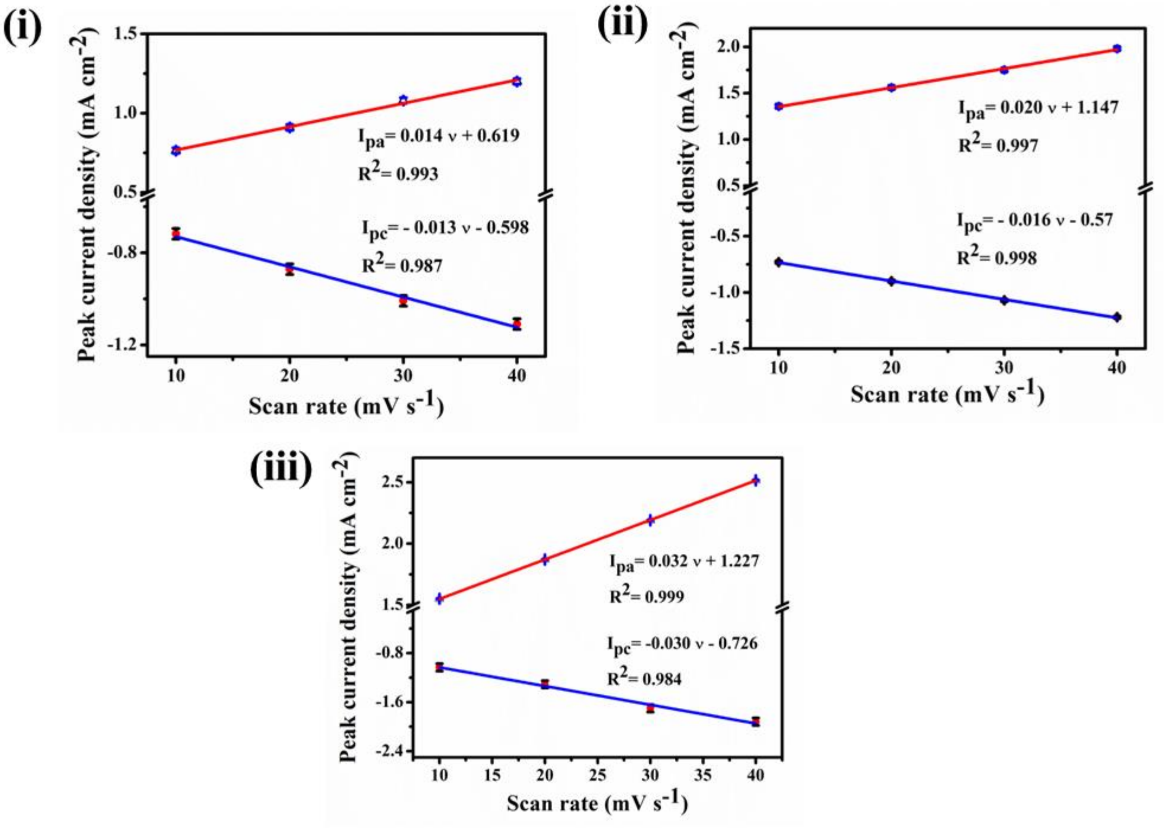

Figure 4.8: *Linear dependence of anodic and cathodic peak current densities vs. scan rate (10-40 mV s^{-1}) for (i) MnO$_2$/ITO, (ii) PEDOT:PSS/MnO$_2$/ITO and (iii) rGO/PEDOT:PSS/MnO$_2$/ITO electrodes.*

The surface coverage of redox species over MnO$_2$/ITO, PEDOT:PSS/MnO$_2$/ITO and rGO/PEDOT:PSS/MnO$_2$/ITO electrodes are found to be 1.44×10^{-8}, 1.92×10^{-8} and 3.34×10^{-8} mol cm^{-2}, respectively, which are comparatively higher than that of the reported values in literature for conducting polymer based electrocatalyst in methanol oxidation [48]. The surface coverage of redox species over rGO/PEDOT:PSS/MnO$_2$/ITO electrode is 1.7 times and 2.3 times larger than that of PEDOT:PSS/MnO$_2$/ITO and MnO$_2$/ITO electrodes, respectively. The higher surface coverage obtained for rGO/PEDOT:PSS/MnO$_2$/ITO electrode can be attributed to large surface area of incorporated rGO nanosheet which provides large number of reactive sites for redox species.

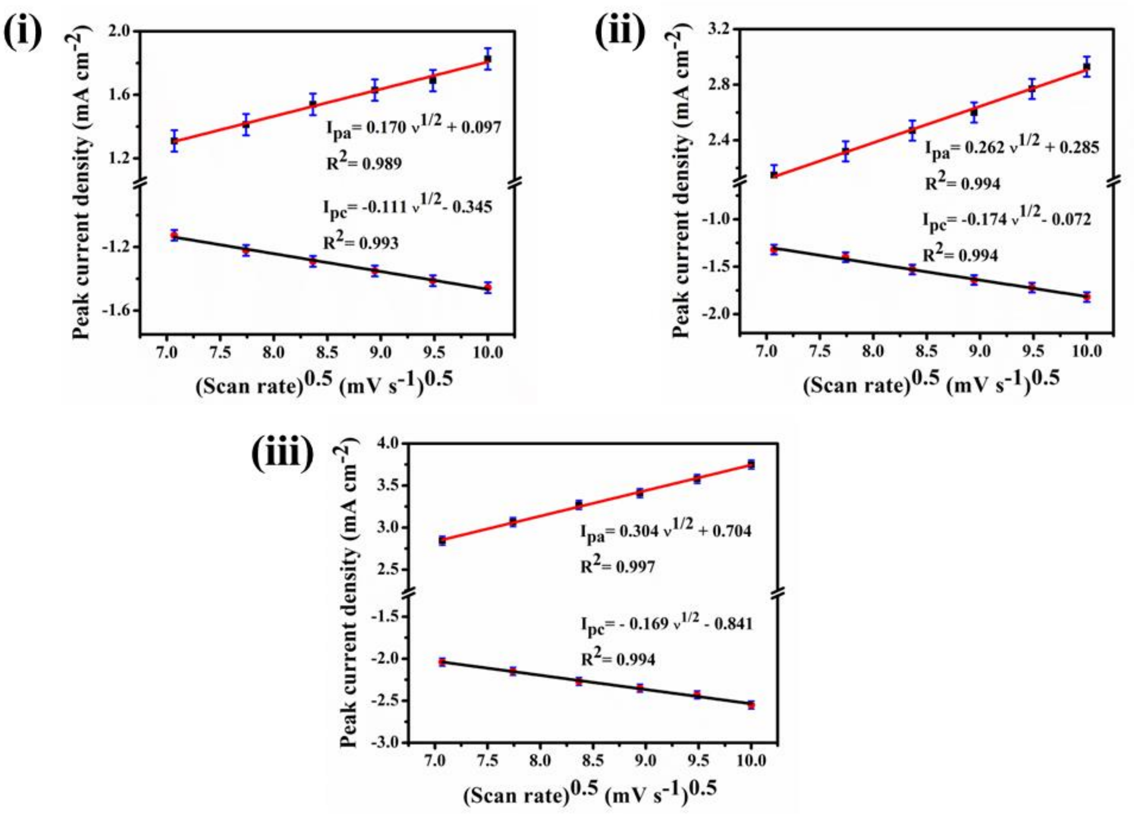

Figure 4.9: *Dependence of anodic and cathodic peak current densities on square root of scan rate (50-100 mV s^{-1}) for (i) MnO$_2$/ITO, (ii) PEDOT:PSS/MnO$_2$/ITO and (iii) rGO/PEDOT:PSS/MnO$_2$/ITO electrodes.*

As shown in Figure 4.9, anodic and cathodic peak current densities are proportional to square root of scan rate at higher scan rates (50-100 mV s^{-1}) implying diffusion controlled process followed by Faradaic reaction. Diffusion capability of hydroxyl ions is determined from the slope of anodic peak currents (I_{pa}) vs. square roots of scan rate ($v^{1/2}$). Usually, a larger slope value implies fast diffusion capability of hydroxyl ions and presence of more number of electroactive MnOOH species over the electrode surface. The anodic slopes of these plots for MnO$_2$/ITO, PEDOT:PSS/MnO$_2$/ITO and rGO/PEDOT:PSS/MnO$_2$/ITO electrodes are obtained to be 0.170, 0.262 and 0.304, respectively. The larger slope for rGO/PEDOT:PSS/MnO$_2$/ITO electrode indicates enhanced diffusion of hydroxyl ions over the electrode surface and thus large number of MnOOH species are formed over rGO/PEDOT:PSS/MnO_2/ITO electrode surface.

4.4.1.2 Variation of anodic peak potential (E_{pa}) and cathodic peak potential (E_{pc}) vs. scan rate (v)

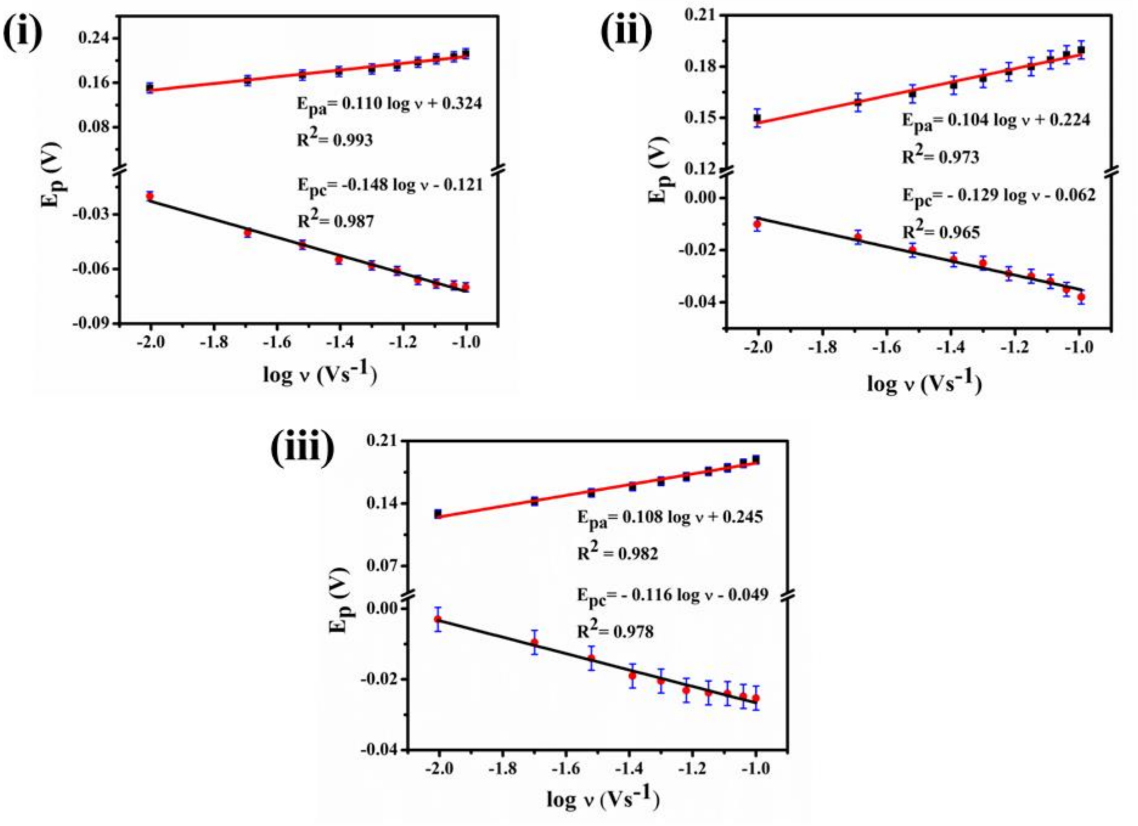

Figure 4.10: *Linear fitted plots of anodic and cathodic peak potentials (E_p) vs. logarithm of scan rate (logv) for (i) MnO_2/ITO, (ii) PEDOT:PSS/MnO_2/ITO and (iii) rGO/PEDOT:PSS/MnO_2/ITO electrodes.*

To understand the reaction kinetics and electron transfer rate between the electrode and electrolyte, determination of heterogeneous rate constant (k_s) and electron transfer coefficient (α) is necessary. According to Laviron's method [49], values of k_s and α can be obtained by plotting anodic and cathodic peak potential (E_p) vs. logarithm of scan rate (logv) using the following equations:

$$E_{pc} = E_0 - 2.3RT\frac{\log\nu}{\alpha nF} \qquad [4.4]$$

$$E_{pa} = E_0 + 2.3RT\frac{\log\nu}{(1-\alpha)nF} \qquad [4.5]$$

$$\mathrm{logk_s} = \alpha \log(1-\alpha) + (1-\alpha)\log\alpha - \log\left(\frac{\mathrm{RT}}{\mathrm{nF}\nu}\right) - \frac{\alpha(1-\alpha)\mathrm{nF}\Delta\mathrm{E_p}}{2.3\mathrm{RT}} \qquad [4.6]$$

Where, E_{pa} is anodic peak potential, E_{pc} is cathodic peak potential, ν is scan rate, n is the number of electrons involved (here n=1), ΔE_p is peak to peak separation and the other terms have their usual meanings. Figure 4.10 shows the plots of anodic and cathodic peak potential (E_p) vs. logν, from which slope can be determined. The calculated values of anodic electron transfer coefficient (α_a), cathodic electron transfer coefficient (α_c) and heterogeneous rate constant (k_s) for all the modified electrodes are tabulated in Table 4.1. As observed from the Table 4.1, values of anodic electron transfer coefficient (α_a) and cathodic electron transfer coefficient (α_c) are not same for all the electrodes, implying that rate limiting step for both oxidation and reduction might not be the same [50]. The higher value of k_s (0.055 cm s^{-1}) at rGO/PEDOT:PSS/MnO_2/ITO electrode indicates that the presence of rGO enhances electron transfer rate between the electrode and electrolyte.

Table 4.1: *Calculated values of anodic electron transfer coefficient (α_a), cathodic electron transfer coefficient (α_c) and heterogeneous rate constant (k_s) of the modified electrodes.*

Electrodes	Anodic electron transfer coefficient (α_a)	Cathodic electron transfer coefficient (α_c)	Heterogeneous rate constant (k_s) (cm s^{-1})
MnO_2/ITO	0.46	0.4	0.038
PEDOT:PSS/MnO_2/ITO	0.43	0.46	0.041
rGO/PEDOT:PSS/MnO_2/ITO	0.45	0.51	0.055

4.4.2 Electrochemical activity of the electrodes toward methanol oxidation

Figure 4.11 (i) shows CVs of all the modified electrodes in presence of 0.5 M methanol at a scan rate 50 mVs^{-1}. The anodic oxidation current density obtained for rGO/PEDOT:PSS/MnO_2/ITO electrode is much higher (56.3 mA cm^{-2}) than that for PEDOT:PSS/MnO_2 electrode (21.5 mA cm^{-2}). Again the onset oxidation potential of rGO/PEDOT:PSS/MnO_2/ITO electrode shifts toward negative side (0.32 V) than that for PEDOT:PSS/MnO_2/ITO electrode (0.35 V). The higher electrochemical performance of rGO/PEDOT:PSS/MnO_2/ITO electrode can be attributed to fine dispersion of PEDOT:PSS coated MnO_2 nanorods over rGO sheets. Electrocatalytic activity of the electrocatalyst depends on the following factors [48]: (i) energy level of the electrocatalyst and electrode material, (ii) charge transfer process and diffusion of ions between the electrode and electrolyte and (iii) the surface structure of electrode. Here the presence of highly porous MnO_2 nanorods makes it accessible for the electrolyte ions and electrons to penetrate deep into the pores of the nanocomposite coated electrode. Thus diffusion becomes easier due to porous morphology of the nanocomposite. Since PEDOT:PSS is p-type semi-conducting polymer [51], the holes present in the polymer during oxidation combine with electrons extracted from the electrolyte and charge transfer takes place through the polymer chain [48]. Again the wrapped rGO nanosheets in ternary nanocomposite enhance the electron transfer rate and number of reaction sites due to its high conductivity and large surface area, respectively.

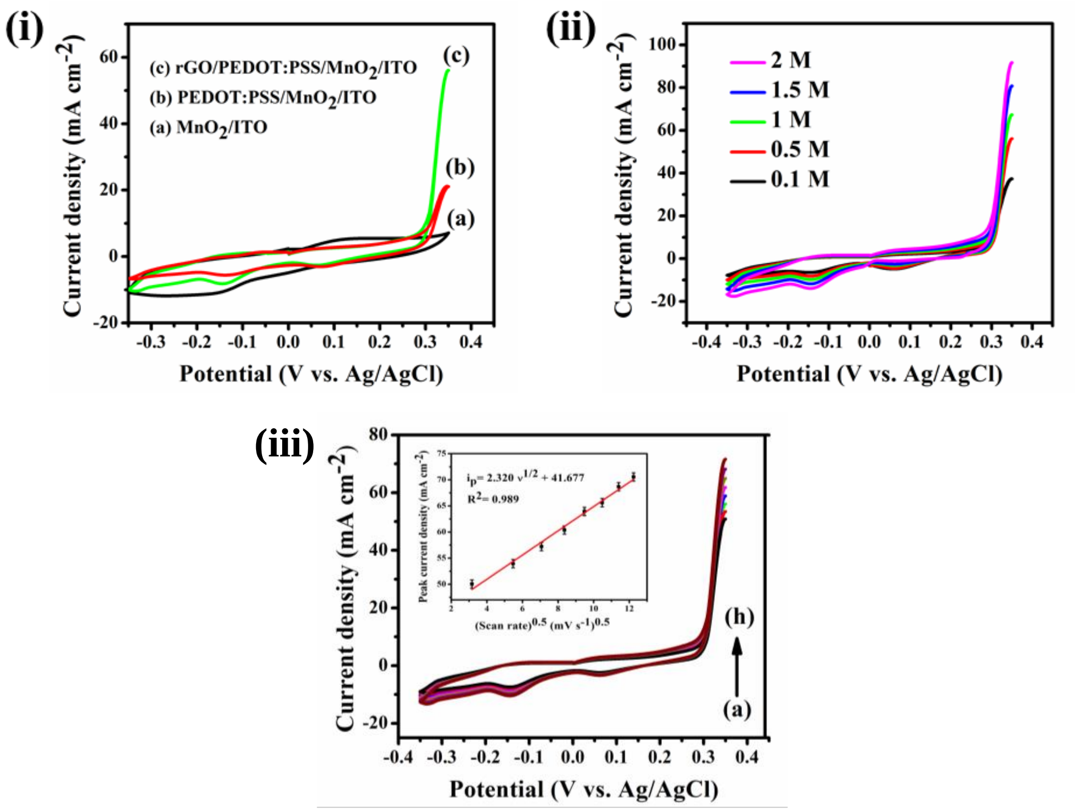

Figure 4.11: *(i) Cyclic voltammograms of (a) MnO_2/ITO, (b) PEDOT:PSS/MnO_2/ITO and (c) rGO/PEDOT:PSS/MnO_2/ITO electrodes in presence of 0.5 M methanol containing in 0.5M NaOH as background electrolyte at a scan rate 50 mV s^{-1}; (ii) Cyclic voltammograms of rGO/PEDOT:PSS/MnO_2/ITO electrode in 0.5 M NaOH solution in presence of 0.1 M, 0.5 M, 1 M, 1.5 M and 2 M methanol at a scan rate 50 mV s^{-1}; (iii) Cyclic voltammograms of rGO/PEDOT:PSS/MnO_2/ITO electrode in presence of 0.5 M methanol at different scan rates (a) 10 mV s^{-1}, (b) 30 mV s^{-1}, (c) 50 mV s^{-1},(d) 70 mV s^{-1},*

(e) 90 mV s^{-1}, (f) 110 mV s^{-1}, (g) 130 mV s^{-1} and (h) 150 mV s^{-1} (Inset shows linear dependence of anodic peak current density on square root of scan rate).

Figure 4.11 (ii) presents the CV curves of rGO/PEDOT:PSS/MnO$_2$/ITO electrode in 0.5 M NaOH solution containing 0.1 M, 0.5 M, 1 M, 1.5 M and 2 M of methanol at scan rate of 50 mV s^{-1}. The possible electro-oxidation mechanism of methanol can be explained by the following reactions [52, 53]:

$$\mathrm{Mn(OH)_2 + OH^- \rightarrow MnOOH + H_2O + e^-} \tag{4.7}$$

$$\mathrm{MnOOH + CH_3OH + \frac{5}{4}\,O_2 \rightarrow Mn(OH)_2 + CO_2 + \frac{3}{2}\,H_2O} \tag{4.8}$$

The typical reaction mechanism corresponds to electro-catalytic (EC$^{/}$) mechanism where electron transfer is followed by catalytic chemical reaction and the system becomes autocatalytic [54, 55]. As observed from Figure 4.11 (ii), a small cathodic peak at 0.06 V appears due to reduction of MnOOH to Mn(OH)$_2$. A thick layer of MnOOH forms during reduction of MnO$_2$ which acts as electron mediator and presence of Mn(OH)$_2$ and MnOOH (electroactive species) are the reason for electrocatalytic activity of Mn based catalyst [53]. The intensity of the cathodic peak at 0.06 V decreases with increase in concentration of methanol, since consumption of MnOOH during oxidation of methanol as shown in equation 4.8, instead of reduction to Mn(OH$_2$) and finally disappears at 2M methanol concentration [56]. The number of reactive sites at the electrode decreases due to adsorption of intermediates produced during methanol oxidation which deteriorates the electrocatalytic activity of the electrode. So the cathodic peak at -0.14 V indicates oxidation of intermediate species and regeneration of reactive sites for further oxidation [45]. This peak becomes more prominent on increase in methanol concentration due to oxidation of large number of intermediates and products. Methanol oxidation mechanism involves two processes: (a) at first adsorption of methanol molecules on the electroactive sites of the electrocatalyst, and (b) subsequent splitting of water molecules from which oxygen is obtained [57]. The poisonous CO formed during methanol oxidation is further oxidized to CO$_2$ by water-gas shift reaction. The water-gas shift reaction involves regenerative redox mechanism where first removal of hydrogen from activated water molecules and then dissociation of hydroxyl ion to form atomic oxygen [57]. The poisonous carbon monoxide reacts with oxygen to form carbon dioxide. Equation 4.8 shows the overall reaction of formation of CO$_2$ from methanol.

Figure 4.11 (iii) depicts the CV curves of rGO/PEDOT:PSS/MnO_2/ITO electrode in 0.5 M methanol solution at scan rates of 10, 30, 50, 70, 90, 110, 130 and 150 mV s^{-1}. Inset shows that anodic peak current density linearly increases with scan rate indicating diffusion controlled process.

4.4.3 Tafel analysis

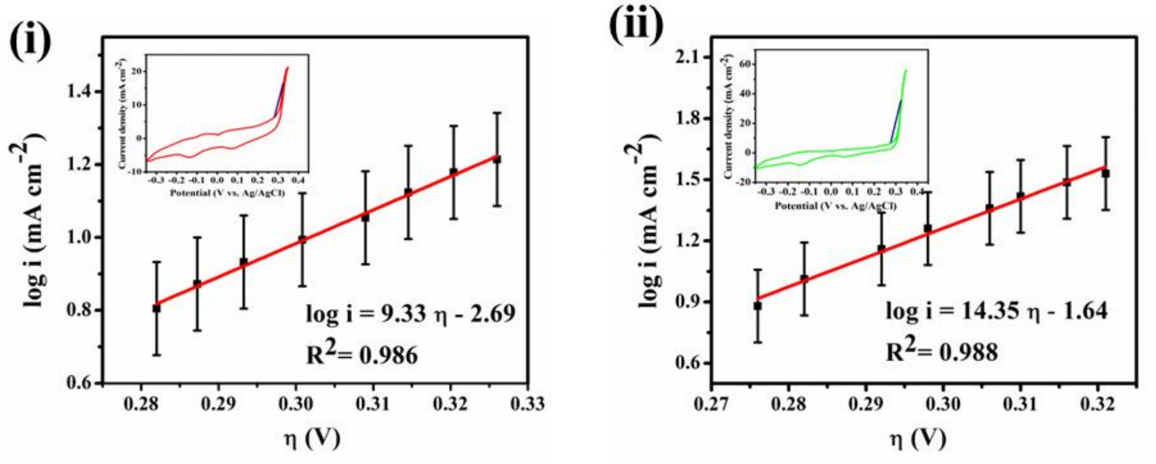

Figure 4.12: *Tafel plots obtained from rising part of the cyclic voltammograms of (i) PEDOT:PSS/MnO_2/ITO and (ii) rGO/PEDOT:PSS/MnO_2/ITO electrodes in presence of 0.5 M methanol at scan rate 50 mV s^{-1}.*

Figures 4.12 (i) and (ii) display Tafel plots (log i vs. η) of PEDOT:PSS/MnO_2/ITO and rGO/PEDOT:PSS/MnO_2/ITO electrodes for methanol oxidation reaction, respectively. As shown in Figure 4.12, data for Tafel plots are obtained from rising part of the CV curves of the electrodes in presence of 0.5 M methanol at a scan rate 50 mV s^{-1}. The calculated values of kinetic parameters obtained from the Tafel slopes are tabulated in Table 4.2. Tafel slope for anodic reaction can be determined by using the following equation [58]:

$$\log \mathrm{i} = \log \mathrm{i}_0 + \frac{\alpha \mathrm{nF}}{2.303\mathrm{RT}}\eta \qquad [4.9]$$

Where, i_0 and α are the exchange current density and electron transfer coefficient of methanol oxidation, respectively. The lower value of Tafel slope (69 mV dec^{-1}) of rGO/PEDOT:PSS/MnO_2/ITO electrode indicates good electrocatalytic activity due to slower increase in overvoltage with increase in current density. Electron transfer coefficient (α) of PEDOT:PSS/MnO_2/ITO and rGO/PEDOT:PSS/MnO_2/ITO electrodes are calculated to be 0.55 and 0.86, respectively. The higher value of α of rGO/PEDOT:PSS/MnO_2/ITO electrode indicates that oxidation is favoured and the larger value of exchange current density (2.29×10^{-2} mA cm^{-2}) of rGO/PEDOT:PSS/MnO_2/ITO electrode suggests lower overvoltage and more stable to external effects.

Table 4.2: *Kinetic parameters of the modified electrodes obtained from Tafel plot.*

Electrodes	Tafel slope (β) (mV dec^{-1})	Electron transfer coefficient (α)	Exchange current density (i_o) (mA cm^{-2})
PEDOT:PSS/MnO_2/ITO	107	0.55	2.04×10^{-3}
rGO/PEDOT:PSS/MnO_2/ITO	69	0.86	2.29×10^{-2}

4.4.4 Chronoamperometry and Cyclic stability test

Figure 4.13 (i) displays the chronoamperometric curves of all the modified electrodes in 0.5 M methanol containing in 0.5 M NaOH for 1 h at 0.32 V. Chronoamperometric analysis shows that rGO/PEDOT:PSS/MnO_2/ITO electrode holds more current density i.e. 50 mA cm^{-2} than that of PEDOT:PSS/MnO_2/ITO (21 mA cm^{-2}) and MnO_2/ITO (1.6 mA cm^{-2}) electrodes, which is in good agreement with CV results. The current retention factor for MnO_2/ITO, PEDOT:PSS/MnO_2/ITO and rGO/PEDOT:PSS/MnO_2/ITO are calculated to be 8.3% 54.2% and 70.3% of initial current, respectively. All the electrodes exhibit sudden decay of current for first few seconds due to formation of double layer capacitance and then slow decay of currents over the whole time range due to CO adsorption on the surface of electrocatalysts [59]. The large surface area of rGO nanosheets may act as active sites for the conversion of intermediates of methanol oxidation such as CO to CO_2 by combining with hydroxyl ions which may regenerate the active sites and maintain the stability of the electrocatalyst.

The stability of the electrodes is also observed by continuous 1000 CV cycles as depicted in Figure 4.13 (ii). rGO/PEDOT:PSS/MnO_2/ITO electrode exhibits cyclic stability upto 1000 CV cycles with current retention factor 74% of initial value at a scan rate 50 mV s^{-1}. The decrement in current is observed due to consumption of methanol and formation of intermediate products. The current retention factor returns to 82% of its initial value when the electrolyte is replaced with fresh 0.5 M methanol containing in 0.5 M NaOH electrolyte. These results suggest that rGO/PEDOT:PSS/MnO_2/ITO electrode exhibits good electrocatalytic activity and long term stability.

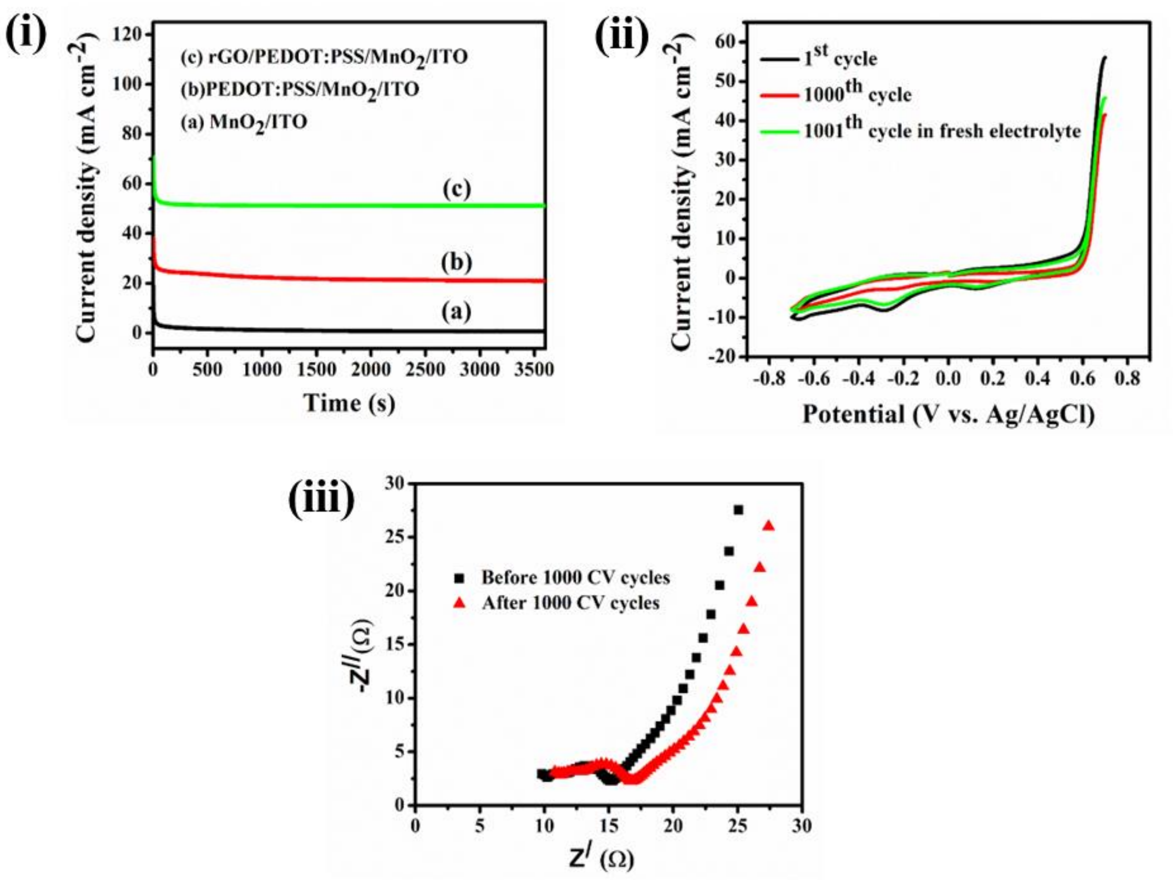

Figure 4.13: *(i) Chronoamperometric curves of (a) MnO_2/ITO, (b) PEDOT:PSS/MnO_2/ITO and (c) rGO/PEDOT:PSS/MnO_2/ITO electrodes at an applied potential of 0.32 V; (ii) Cyclic stability of rGO/PEDOT:PSS/MnO_2/ITO electrode upto 1000 CV cycles at a scan rate 50 mV s^{-1}; (iii) Nyquist plots of rGO/PEDOT:PSS/MnO_2/ITO electrode before and after 1000 CV cycles in presence of 0.5 M methanol containing in 0.5 M NaOH electrolyte.*

4.4.5 Electrochemical impedance spectroscopy measurements after cyclic stability test

Figure 4.13 (iii) depicts the Nyquist plots of rGO/PEDOT:PSS/MnO_2/ITO electrode before and after 1000 CV cycles in presence of 0.5 M methanol containing in 0.5 M NaOH solution. In Nyquist plot, the initial point of the semi-circle on x-axis, diameter of the semi-circle in higher frequency side and the straight line in lower frequency side define solution resistance (R_S), charge transfer resistance (R_{ct}) and Warburg impedance (W), respectively. The slight change in charge transfer resistance from 5.05 Ω to 6.13 Ω and small inclination of Warburg impedance line towards lower angle side after 1000 CV cycles as observed in Figure 4.13 (iii) indicate better stability of the electrode. Increase in charge transfer resistance and inclination of Warburg impedance line may be due to formation of oxidation intermediates and change in diffusion path length in presence of methanol [45, 52].

4.4.6 Characterizations after cyclic stability test

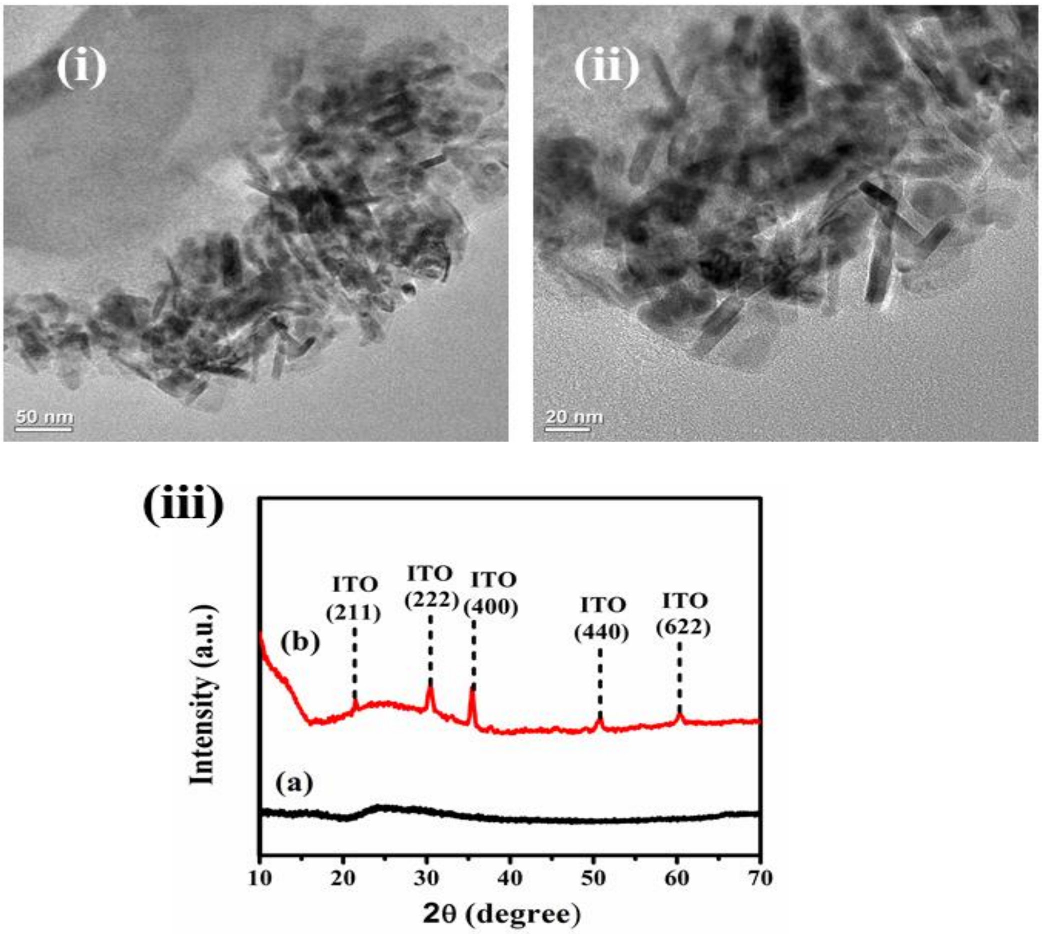

Figure 4.14: *TEM micrographs of rGO/PEDOT:PSS/MnO_2 nanocomposite after 1000 CV cycles in presence of 0.5 M methanol containing in 0.5 M NaOH at resolutions of (i) 50 nm and (ii) 20 nm, (iii) XRD patterns of (a) rGO/PEDOT:PSS/MnO_2 nanocomposite and (b) rGO/PEDOT:PSS/MnO_2/ITO electrode after 1000 CV cycles in 0.5 M methanol containing solution.*

TEM, XRD and XPS measurements of rGO/PEDOT:PSS/MnO_2/ITO electrode have been done after 1000 CV cycles to investigate morphology, structure and composition of the electrode. The TEM images (Figure 4.14 (i) and (ii)) reveal that MnO_2 nanorods appear even after 1000 CV cycles however diameter and length of the nanorods decrease that lie within the range of 7-15 nm and 30-50 nm, respectively. The XRD pattern of rGO/PEDOT:PSS/MnO_2/ITO electrode has been recorded after 1000 CV cycles in presence of 0.5 M methanol containing in 0.5 M NaOH electrolyte. Figure 4.14 (iii) shows that the characteristic broad peak of rGO/PEDOT:PSS/MnO_2 nanocomposite appears around 24.5° even after cyclic stability test for 1000 CV cycles indicating structural stability of the ternary nanocomposite. The intense peaks of ITO glasses have been observed at 21.5°, 30.4°, 35.6°, 50.7° and 60.3° attributing to (211), (222), (400), (440) and (622) planes, respectively.

In the survey spectrum (Figure 4.15 (i)) of rGO/PEDOT:PSS/MnO_2/ITO, the peaks corresponding to In 4d, Sn 3d and In 3p bands of ITO are observed [60]. The intensity of Mn 2p peak slightly decreases after stability test as shown in Figure 4.15 (ii). The continuous transition between $Mn(OH)_2$ and MnOOH, which act as electroactive media during oxidation process of methanol causes consumption of Mn species. Therefore, the intensity of Mn 2p spectrum decreases after continuous 1000 CV cycling. In C 1s spectrum (Figure 4.15 (iii)), the intensity of deconvoluted peak at 284.8 eV corresponding to C-C bond decreases due to consumption of carbon content in rGO/PEDOT:PSS/MnO_2/ITO electrode during 1000 CV cycling and a satellite peak appears at 291.2 eV. The intensity of deconvoluted peak at 530.5 eV associated with Mn-O-H group in O 1s spectrum decreases as shown in Figure 4.15 (iv) due to consumption of manganese ions during methanol oxidation and broad peak appears at 534.9 eV upon continuous CV cycling upto 1000 cycles and that corresponds to sodium Auger peak (NaKLL) indicating the presence of significant amount of Na^+ on the electrode surface. As shown in Figure 4.15 (v), the intensity of peak associated with PEDOT in S 2p spectrum diminishes due to disintegration of PEDOT:PSS film after stability test. A small intense peak at 1073 eV arises in the survey spectrum (Figure 4.15 (i)) of rGO/PEDOT:PSS/MnO_2/ITO electrode after continuous cycling test indicating the adsorption of Na^+ ions from the electrolyte onto the electrode surface.

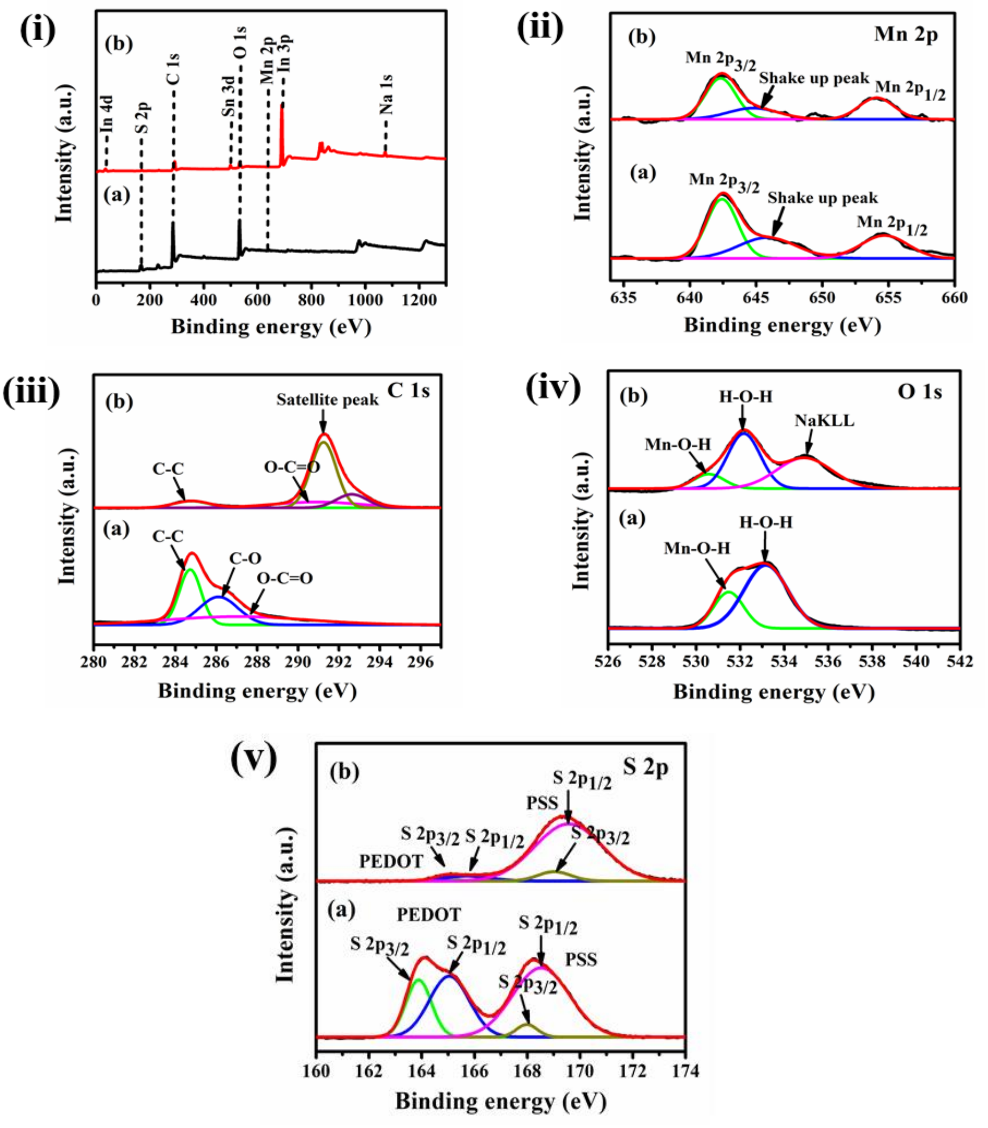

Figure 4.15: *(i) Survey spectra of (a) rGO/PEDOT:PSS/MnO_2 nanocomposite (b) rGO/PEDOT:PSS/MnO_2/ITO electrode after 1000 CV cycles. Core-level XPS spectra of (ii) Mn 2p, (iii) C 1s, (iv) O 1s (v) S 2p regions of (a) rGO/PEDOT:PSS/MnO_2 nanocomposite (b) rGO/PEDOT:PSS/MnO_2/ITO electrode after 1000 CV cycles in 0.5 M methanol containing in 0.5 M NaOH solution.*

4.5 Summary

A ternary nanocomposite rGO/PEDOT:PSS/MnO_2 has been synthesized and its morphological, structural, electrochemical behaviour and electrocatalytic properties toward methanol oxidation have been investigated. SEM and TEM images reveal that PEDOT:PSS coated MnO_2 nanorods are wrapped within rGO nanosheets. The higher surface area (190 m^2 g^{-1}) and mesoporous structure (pore volume 0.55 cm^3 g^{-1}) of the ternary nanocomposites enhance the penetration of ions into deep pores leading to improved contact between electrolyte and electroactive sites of the electrocatalyst. rGO/PEDOT:PSS/MnO_2/ITO electrode exhibits enhanced anodic current density of 56.3 mA cm^{-2} and lower onset potential of 0.32 V in presence of 0.5 M methanol containing in 0.5 M NaOH solution at a scan rate of 50 mV s^{-1}. On increase in methanol concentration, anodic current density gradually increases and cathodic current density decreases due to consumption of MnOOH electroactive species during oxidation, although intensity of reverse peak due to oxidation of intermediate species increases due to more production of carbonaceous intermediates at higher methanol concentration. rGO/PEDOT:PSS/MnO_2/ITO electrode exhibits enhanced stability with current density 50 mA cm^{-2} upto 1 h and higher cyclic stability of 74% upto 1000 CV cycles. The TEM micrographs show that MnO_2 nanorod structures appear even after 1000 CV cycles however diameter and length of the nanorods decrease due to continuous CV cycling. The characteristic broad XRD peak of rGO/PEDOT:PSS/MnO_2 nanocomposite appears even after stability test. A small peak appears at 1073 eV in the survey spectra of rGO/PEDOT:PSS/MnO_2/ITO electrode indicating the presence of significant amount of Na^+ on the electrode surface. Moreover, the changes in core spectra of Mn 2p, C 1s, O 1s and S 2p peak after 1000 CV cycling suggest the consumption of Manganese species, carbon content and degradation of PEDOT:PSS film, respectively.

The enhanced electrocatalytic activity of rGO/PEDOT:PSS/MnO_2/ITO electrode can be attributed to (i) the presence of deep open pores between the nanorods which act as reactive sites for electrolyte diffusion, (ii) PEDOT:PSS, the p-type conducting polymer acts as matrix which donates holes for electro-oxidation process and (iii) presence of rGO enhances the electron transfer rate and it also provides larger surface area for oxidation of methanol molecules. Synergetic effects of all these three materials lead to the enhancement of electrocatalytic property of rGO/PEDOT:PSS/MnO_2/ITO electrode.

4.6 References

[1] Zhu, Y., Cao, C., Tao, S., Chu, W., Wu, Z. and Li, Y. Ultrathin nickel hydroxide and oxide nanosheets: synthesis, characterizations and excellent supercapacitor performances. *Scientific reports*, 4(1):1-7, 2014.

[2] Pattanayak, P., Pramanik, N., Kumar, P. and Kundu, P.P. Fabrication of cost-effective non-noble metal supported on conducting polymer composite such as copper/polypyrrole graphene oxide (Cu_2O/PPy-GO) as an anode catalyst for methanol oxidation in DMFC. *International journal of hydrogen energy*, 43(25):11505-11519, 2018.

[3] Fotouhi, L., Fathali, N. and Ehsani, A. ZnO/Polytyramine nanocomposite film: Facile electrosynthesis and high performance electrocatalytic activity toward methanol oxidation. *International Journal of Hydrogen Energy*, 43(14):6987-6996, 2018.

[4] Li, L., Scott, K. and Yu, E.H. A direct glucose alkaline fuel cell using MnO_2-carbon nanocomposite supported gold catalyst for anode glucose oxidation. *Journal of power sources*, 221:1-5, 2013.

[5] Rajeshkhanna, G. and Rao, G.R. Micro and nano-architectures of Co_3O_4 on Ni foam for electro-oxidation of methanol. *International Journal of Hydrogen Energy*, 43(9), 4706-4715, 2018.

[6] Liu, Y., Zhang, X., He, D., Ma, F., Fu, Q. and Hu, Y. An amperometric glucose biosensor based on a MnO_2/graphene composite modified electrode. *RSC advances*, 6(22):18654-18661, 2016.

[7] Alfaruqi, M.H., Islam, S., Gim, J., Song, J., Kim, S., Pham, D.T., Jo, J., Xiu, Z., Mathew, V. and Kim, J. A high surface area tunnel-type α-MnO_2 nanorod cathode by a simple solvent-free synthesis for rechargeable aqueous zinc-ion batteries. *Chemical Physics Letters*, 650:64-68, 2016.

[8] Yousefi, T., Golikand, A.N., Mashhadizadeh, M.H. and Aghazadeh, M. Facile synthesis of α-MnO_2 one-dimensional (1D) nanostructure and energy storage ability studies. *Journal of Solid State Chemistry*, 190:202-207, 2012.

[9] Chen, J., Jia, C. and Wan, Z. The preparation and electrochemical properties of MnO_2 /poly(3,4-ethylenedioxythiophene)/multiwalled carbon nanotubes hybrid nanocomposite and its application in a novel flexible micro-supercapacitor. *Electrochimica Acta*, 121:49-56, 2014.

[10] Tang, P., Han, L. and Zhang, L. Facile synthesis of graphite/PEDOT/MnO_2 composites on commercial supercapacitor separator membranes as flexible and high-performance supercapacitor electrodes. *ACS applied materials & interfaces*, 6(13):10506-10515, 2014.

[11] Ko, I.H., Kim, S.J., Lim, J., Yu, S.H., Ahn, J., Lee, J.K. and Sung, Y.E. Effect of PEDOT:PSS coating on manganese oxide nanowires for lithium ion battery anodes. *Electrochimica Acta*, 187:340-347, 2016.

[12] Sen, P., De, A., Chowdhury, A.D., Bandyopadhyay, S.K., Agnihotri, N. and Mukherjee, M. Conducting polymer based manganese dioxide nanocomposite as supercapacitor. *Electrochimica Acta*, 108:265-273, 2013.

[13] Liu, R., Duay, J. and Lee, S.B. Redox exchange induced MnO_2 nanoparticle enrichment in poly (3, 4-ethylenedioxythiophene) nanowires for electrochemical energy storage. *Acs Nano*, 4(7):4299-4307, 2010.

[14] Hou, Y., Cheng, Y., Hobson, T. and Liu, J. Design and synthesis of hierarchical MnO_2 nanospheres/carbon nanotubes/conducting polymer ternary composite for high performance electrochemical electrodes. *Nano letters*, 10(7):2727-2733, 2010.

[15] Lee, C., Wei, X., Kysar, J.W. and Hone, J. Measurement of the elastic properties and intrinsic strength of monolayer graphene. *Science*, 321(5887):385-388, 2008.

[16] Stoller, M.D., Park, S., Zhu, Y., An, J. and Ruoff, R.S. Graphene-based ultracapacitors. *Nano letters*, 8(10):3498-3502, 2008.

[17] Baronia, R., Goel, J., Tiwari, S., Singh, P., Singh, D., Singh, S.P. and Singhal, S.K. Efficient electro-oxidation of methanol using PtCo nanocatalysts supported reduced graphene oxide matrix as anode for DMFC. *International Journal of Hydrogen Energy*, 42(15):10238-10247, 2017.

[18] Ehsani, A., Jaleh, B. and Nasrollahzadeh, M. Electrochemical properties and electrocatalytic activity of conducting polymer/copper nanoparticles supported on reduced graphene oxide composite. *Journal of Power Sources*, 257:300-307, 2014.

[19] Glass, D.E., Galvan, V. and Prakash, G.S. The effect of annealing temperature on nickel on reduced graphene oxide catalysts on urea electrooxidation. *Electrochimica Acta*, 253:489-497, 2017.

[20] Das, A.K., Layek, R.K., Kim, N.H., Jung, D. and Lee, J.H. Reduced graphene oxide (RGO)-supported $NiCo_2O_4$ nanoparticles: an electrocatalyst for methanol oxidation. *Nanoscale*, 6(18):10657-10665, 2014.

[21] Hareesh, K., Shateesh, B., Joshi, R.P., Williams, J.F., Phase, D.M., Haram, S.K. and Dhole, S.D. Ultra high stable supercapacitance performance of conducting polymer coated MnO_2 nanorods/rGO nanocomposites. *RSC advances*, 7(32):20027-20036, 2017.

[22] Wu, T., Wang, C., Mo, Y., Wang, X., Fan, J., Xu, Q. and Min, Y. A ternary composite with manganese dioxide nanorods and graphene nanoribbons embedded in a polyaniline matrix for high-performance supercapacitors. *RSC advances*, 7(53):33591-33599, 2017.

[23] Yan, D., Liu, Y., Li, Y., Zhuo, R., Wu, Z., Ren, P., Li, S., Wang, J., Yan, P. and Geng, Z. Synthesis and electrochemical properties of MnO_2/rGO/PEDOT:PSS ternary composite electrode material for supercapacitors. *Materials Letters*, 127:53-55, 2014.

[24] Devi, M. and Kumar, A. In-situ reduced graphene oxide nanosheets-polypyrrole nanotubes nanocomposites for supercapacitor applications. *Synthetic Metals*, 222:318-329, 2016.

[25] Zhao, Y., Song, X., Song, Q. and Yin, Z. A facile route to the synthesis copper oxide/reduced graphene oxide nanocomposites and electrochemical detection of catechol organic pollutant. *CrystEngComm*, 14(20):6710-6719, 2012.

[26] Kumar, S. and Kumar, A. Chemically derived luminescent graphene oxide nanosheets and its sunlight driven photocatalytic activity against methylene blue dye. *Optical Materials*, 62:320-327, 2016.

[27] Emiru, T.F. and Ayele, D.W. Controlled synthesis, characterization and reduction of graphene oxide: A convenient method for large scale production. *Egyptian Journal of Basic and Applied Sciences*, 4(1):74-79, 2017.

[28] Haldorai, Y., Giribabu, K., Hwang, S.K., Kwak, C.H., Huh, Y.S. and Han, Y.K. Facile synthesis of α-MnO_2 nanorod/graphene nanocomposite paper electrodes using a 3D precursor for supercapacitors and sensing platform to detect 4-nitrophenol. *Electrochimica Acta*, 222:717-727, 2016.

[29] Zhao, Q., Jamal, R., Zhang, L., Wang, M. and Abdiryim, T. The structure and properties of PEDOT synthesized by template-free solution method. *Nanoscale research letters*, 9(1):1-9, 2014.

[30] Agnihotri, N., Sen, P., De, A. and Mukherjee, M. Hierarchically designed PEDOT encapsulated graphene-MnO_2 nanocomposite as supercapacitors. *Materials Research Bulletin*, 88:218-225, 2017.

[31] Mu, B., Zhang, W., Shao, S. and Wang, A. Glycol assisted synthesis of graphene-MnO_2-polyaniline ternary composites for high performance supercapacitor electrodes. *Physical Chemistry Chemical Physics*, 16(17):7872-7880, 2014.

[32] Yu, L., Gan, M., Ma, L., Huang, H., Hu, H., Li, Y., Tu, Y., Ge, C., Yang, F. and Yan, J. Facile synthesis of MnO_2/polyaniline nanorod arrays based on graphene and its electrochemical performance. *Synthetic metals*, 198:167-174, 2014.

[33] Yoon, S.B. and Kim, K.B. Effect of poly (3, 4-ethylenedioxythiophene)(PEDOT) on the pseudocapacitive properties of manganese oxide (MnO_2) in the PEDOT/MnO_2/multiwall carbon nanotube (MWNT) composite. *Electrochimica Acta*, 106:135-142, 2013.

[34] Shah, H.U., Wang, F., Javed, M.S., Ahmad, M.A., Saleem, M., Zhan, J., Khan, Z.U.H. and Li, Y. In-situ growth of MnO_2 nanorods forest on carbon textile as efficient electrode material for supercapacitors. *Journal of Energy Storage*, 17:318-326, 2018.

[35] Ram, J., Singh, R.G., Singh, F., Kumar, V., Chauhan, V., Gupta, R., Kumar, U., Yadav, B.C. and Kumar, R. Development of WO_3-PEDOT:PSS hybrid nanocomposites based devices for liquefied petroleum gas (LPG) sensor. *Journal of Materials Science: Materials in Electronics*, 30(14):13593-13603, 2019.

[36] Xu, B., Gopalan, S.A., Gopalan, A.I., Muthuchamy, N., Lee, K.P., Lee, J.S., Jiang, Y., Lee, S.W., Kim, S.W., Kim, J.S. and Jeong, H.M. Functional solid additive modified PEDOT:PSS as an anode buffer layer for enhanced photovoltaic performance and stability in polymer solar cells. *Scientific Reports*, 7(1):1-13, 2017.

[37] Nguyen, T.P. and De Vos, S.A. An investigation into the effect of chemical and thermal treatments on the structural changes of poly(3,4-ethylenedioxythiophene)/polystyrenesulfonate and consequences on its use on indium tin oxide substrates. *Applied Surface Science,* 221(1-4):330-339, 2004.

[38] Ferrari, A.C. and Basko, D.M. Raman spectroscopy as a versatile tool for studying the properties of graphene. *Nature nanotechnology*, 8(4):235-246, 2013.

[39] Ranjan, P., Agrawal, S., Sinha, A., Rao, T.R., Balakrishnan, J. and Thakur, A.D. A low-cost non-explosive synthesis of graphene oxide for scalable applications. *Scientific Reports*, 8: 12007, 2018.

[40] Ngo, Y.L.T., Sui, L., Ahn, W., Chung, J.S. and Hur, S.H. $NiMn_2O_4$ spinel binary nanostructure decorated on three-dimensional reduced graphene oxide hydrogel for bifunctional materials in non-enzymatic glucose sensor. *Nanoscale*, 9(48):19318-19327, 2017.

[41] Lee, S.B., Lee, S.M., Park, N.I., Lee, S. and Chung, D.W. Preparation and characterization of conducting polymer nanocomposite with partially reduced graphene oxide. *Synthetic Metals*, 201:61-66, 2015.

[42] Lawrence, M. and Jiang, Y. Porosity, pore size distribution, micro-structure. In *Bio-aggregates based building materials*, pages 39-71, ISBN: 978-94-024-1030-3. Springer, Dordrecht, 2017.

[43] Zhong, J., Yi, F., Gao, A., Shu, D., Huang, Y., Li, Z., Zhu, W., He, C., Meng, T. and Zhao, S. Preparation of 3D reduced graphene oxide/MnO_2 nanocomposites through a vacuum-impregnation method and their electrochemical capacitive behavior. *ChemElectroChem*, 4(5):1088-1094, 2017.

[44] Zhang, H., Gu, J., Tong, J., Hu, Y., Guan, B., Hu, B., Zhao, J. and Wang, C. Hierarchical porous MnO_2/CeO_2 with high performance for supercapacitor electrodes. *Chemical Engineering Journal*, 286:139-149, 2016.

[45] Thorat, G.M., Jadhav, H.S. and Seo, J.G. Bi-functionality of mesostructured $MnCo_2O_4$ microspheres for supercapacitor and methanol electro-oxidation. *Ceramics International*, 43(2):2670-2679, 2017.

[46] Pawar, S.M., Kim, J., Inamdar, A.I., Woo, H., Jo, Y., Pawar, B.S., Cho, S., Kim, H. and Im, H. Multi-functional reactively-sputtered copper oxide electrodes for supercapacitor and electro-catalyst in direct methanol fuel cell applications. *Scientific reports*, 6(1):1-9, 2016.

[47] Wang, W., Li, R., Zhang, R., Ma, J. and Wang, B. Electrocatalytic oxidation of methanol on glassy carbon electrode modified with nickel–manganese salen complexes encapsulated in mesoporous zeolite A. *Journal of Electroanalytical Chemistry*, 742: 10-121, 2015.

[48] Ehsani, A., Mahjani, M.G., Jafarian, M. and Naeemy, A. Electrosynthesis of polypyrrole composite film and electrocatalytic oxidation of ethanol. *Electrochimica acta*, 71:128-133, 2012.

[49] Laviron, E.J.J. General expression of the linear potential sweep voltammogram in the case of diffusionless electrochemical systems. *Journal of Electroanalytical Chemistry and Interfacial Electrochemistry*, 101(1):19-28, 1979.

[50] Luo, H., Shi, Z., Li, N., Gu, Z. and Zhuang, Q. Investigation of the electrochemical and electrocatalytic behavior of single-wall carbon nanotube film on a glassy carbon electrode. *Analytical Chemistry*, 73(5):915-920, 2001.

[51] Sharma, B.K., Khare, N. and Ahmad, S. A ZnO/PEDOT: PSS based inorganic/organic hetrojunction. *Solid State Communications*, 149(19-20):771-774, 2009.

[52] Jadhav, H.S., Roy, A., Chung, W.J. and Seo, J.G. Free standing growth of $MnCo_2O_4$ nanoflakes as an electrocatalyst for methanol electro-oxidation. *New Journal of Chemistry*, 41(24):15058-15063, 2017.

[53] Yuan, L.S., Zheng, Y.X., Jia, M.L., Zhang, S.J., Wang, X.L. and Peng, C. Nanoporous nickel-copper-phosphorus amorphous alloy film for methanol electro-oxidation in alkaline medium. *Electrochimica Acta*, 154:54-62, 2015.

[54] Mirčeski, V. and Gulaboski, R. Surface Catalytic Mechanism in Square-Wave Voltammetry. *Electroanalysis: An International Journal Devoted to Fundamental and Practical Aspects of Electroanalysis*, 13(16):1326-1334, 2001.

[55] Ojani, R., Raoof, J.B. and Zamani, S. A novel voltammetric sensor for amoxicillin based on nickel–curcumin complex modified carbon paste electrode. *Bioelectrochemistry*, 85:44-49, 2012.

[56] Azizi, S.N., Ghasemi, S. and Chiani, E. Nickel/mesoporous silica (SBA-15) modified electrode: an effective porous material for electrooxidation of methanol. *Electrochimica Acta*, 88:463-472, 2013.

[57] Iwasita, T. Electrocatalysis of methanol oxidation. *Electrochimica Acta*, 47(22-23):3663-3674, 2002.

[58] Popov, B.N. *Corrosion engineering: principles and solved problems*. Elsevier, 2015.

[59] Hao, Y., Wang, X., Zheng, Y., Shen, J., Yuan, J., Wang, A.J., Niu, L. and Huang, S. Uniform Pt nanoparticles incorporated into reduced graphene oxides with MoO_3 as advanced anode catalysts for methanol electro-oxidation. *Electrochimica Acta*, 198:127-134, 2016.

[60] Jeon, J.S., Yu, I.K., Kim, W. and Choi, S.H. Electrocatalytic oxidation of methanol by a polymeric Ni complex-modified electrode prepared by a one-step cold-plasma process. *Frontiers in Chemistry*, 8:595616, 2020.